이학박사학위논문

자가정렬된 인듐 주석 산화물 나노육면체에서의 전기화학적 구조 효과와 니켈 철산화물에서의 음이온 효과

Geometric Effect on Electron Transfer at Self-assembled Indium Tin Oxide Nanocubes and Anionic Effect at Nickel Iron Oxides

2023년 2월

서울대학교 대학원
화학부 전기분석화학전공

황대웅

Ph.D. Dissertation

Geometric Effect on Electron Transfer at Self-assembled Indium Tin Oxide Nanocubes and Anionic Effect at Nickel Iron Oxides

February 2023

Graduate School of Chemistry
Seoul National University
Major : Electrochemistry

Dae-Woong Hwang

Geometric Effect on Electron Transfer at Self-assembled Indium Tin Oxide Nanocubes and Anionic Effect at Nickel Iron Oxides

지도교수 정 택 동

이 논문을 이학박사 학위논문으로 제출함
2023 년 2 월

서울대학교 대학원
화학부 전기분석화학전공

황대웅

황대웅의 이학박사 학위논문을 인준함
2023 년 2 월

위 원 장	임 종 우	(인)
부위원장	정 택 동	(인)
위 원	이 동 환	(인)
위 원	홍 병 희	(인)
위 원	김 양 래	(인)

Abstract

With the aggravating disasters caused by severe climate change, resource monopoly and ongoing-wars, the globe is in dire need for rapidly shift from fossil fuel-based technology into greener, more sustainable energy technology, such as water electrolysis and energy storage devices. In order to achieve such goals, development of highly efficient, yet affordable electrocatalysts must be realized. In order to produce a good electrocatalyst, one must understand fundamental aspects of the catalyst's electrochemical properties. In this dissertation, two very important aspects of an electrocatalyst will be discussed.

In the first part, enhanced catalytic activity originating from the structural effects in nanoporous electrodes is elaborated. Uniform indium tin oxide (ITO) nanocubes with defined structures was synthesized. Then, nanoporous electrodes composed of self-assembly using ITO nanocube as a building block was fabricated. The self-assembly of nanocubes formed small clusters with uniform pores between the edges of the nanocubes, while random aggregation of the small self-assembled clusters created multimodal structure easily with little effort. It was observed that the simple, outer-sphere one electron-transfer reaction of iron ions was greatly improved on the ITO nanoporous electrodes when compared with the flat ITO electrodes. Such enhancement was attributed to the geometric effect of nanoporous electrode. However, in case of multi-electron, inner-sphere redox reactions such as ascorbic acid oxidation and oxygen reduction reaction, the effect of geometry was largely absent due to inert nature of ITO. These findings provided insights in fabricating better electrocatalysts that both geometry and material of the catalyst plays important role in determining the catalytic activity.

In the second part, effect of anions on the anodic electrodeposition of nickel iron oxide was examined. Nickel iron oxide is a promising catalyst material for alkaline oxygen evolution reaction. Although anodic deposition is beneficial for its preparation, anodically deposited nickel iron oxide fabricated previously by various research groups could not realize the full

potential of the electrocatalyst material. The anodic deposition of nickel iron oxide was thoroughly studied using electroanalytical techniques combined with an electrochemical quartz crystal microbalance. In particular, the effects of anions were investigated to determine their influence on the formation of a nickel iron oxide film during the anodic deposition process. The results showed that anodic deposition was sensitive to the counter anions of the metal precursors and electrolyte. Also, the anions not only provide buffering to retain the solution pH but also play a significant role in scavenging the surface protons to facilitate the growth of the catalyst film. A modified synthetic protocol for anodically deposited nickel iron oxide electrocatalysts with excellent for water oxidation was established. The resultant nickel iron oxide exhibited one of the best reported performances. These findings presented important but previously neglected aspects of anodic deposition, providing implications for nonprecious metal electrocatalysts.

Keyword : electrocatalyst, nanoporous electrode, electrokinetics, anion effect

Student Number : 2011-20313

Table of Contents

List of Figures

Figure 1.7 Overall scheme of ITO nanocube post-treatment and fabrication of nanoporous ITO nanocube electrode.

Figure 1.8 TEM images of morphological change in ITO nanocubes (A) before heat treatment and (B) after heat treatment. Slight change in nanocube morphology and size was observed as a result of heat treatment

Figure 1.9 (A) SEM and (B) TEM images of ITO nanocube used for electrochemical studies. (C) A higher magnification TEM image of self-assembled ITO nanocubes, showing structurally defined pore created by self-assembly. (D~F) SEM images of self-assembled ITO nanocube electrode, which (D) 20 μg, (E) 50 μg and (F) 100 μg of ITO nanocube was drop-casted onto ITO glass substrate.

Figure 1.10 (A) Cyclic voltammograms at bare ITO electrode and nanoporous ITO nanocube electrodes with different ITO loading in 0.1 M Na_2SO_4 (pH 7) solution and (B) Relationship between current density and scan rate obtained from data of (A). Cyclic voltammogram of (C) 1 mM $Ru(NH_3)_6^{2+}$ and (D) 1mM $Fe(CN)_6^{2+}$ in 0.1 M Na_2SO_4 (pH 7) solution. The current in these voltammograms is normalized by the geometric surface area (GSA). Scan rate = 50 mVs^{-1}.

Figure 1.11. Cyclic voltammograms of $Fe^{2+/3+}$ in 0.1 M H_2SO_4 and 0.1 M Na_2SO_4 solution on ITO nanocube electrodes. The current density was normalized with GSA. Scan rate = 50 $mV\ s^{-1}$.

Figure 1.12 (A) Nyquist plots of $Fe^{2+/3+}$ redox system on the bare and nanoporous ITO electrodes. (B) Zoomed in view of the Nyquist plot (A) for better comparison of nanoporous nanocube electrodes with different loadings. The impedance in (A) and (B) was normalized with geometric surface area (GSA). (C) Nyquist plot of $Fe^{2+/3+}$ redox system on the ITO nanocube electrodes normalized with electrochemical surface area (ECSA). (D) Randles

circuit that was used to fit the EIS data.

Figure 1.13 Cyclic voltammogram of 1 mM ascorbic acid in 0.1 M $NaClO_4$ at pH 7 on bare and nanoporous ITO electrodes, which the current was normalized with (A) GSA and (B) ESCA. (C) Cyclic voltammogram where anodic peak current was subtracted by respective capacitive current, then normalized to 1. (D) Nyquist plot for ascorbic acid oxidation on bare and nanoporous ITO electrodes.

Figure 1.14 Linear sweep voltammograms of ORR on bare and nanoporous ITO electrodes where current was normalized with (A) GSA and (B) ESCA. Nyquist Plots of ORR on the same electrodes with impedance normalized with (C) GSA and (D) ESCA. The ORR experiments were carried out in 0.1 M H_2SO_4.

Figure 2.1. CVs and mass change profiles of 0.1 M NaOAc solution containing (a, d) 16 mM Ni(II) (green), (b, e) 5 mM Fe(II) (orange), and (c, f) 16 mM Ni(II) + 5 mM Fe(II) (red). CV and mass change profile of 0.1 M NaOAc solution are depicted in black in (a–f). pH of each solution is 5.3. Potentiostatic deposition in (b, e, f) are conducted at potentials denoted by dashed lines in (a, c, e). Arrows in (a) indicate scan direction.

Figure 2.2. Consecutive cyclic voltammograms of 0.1 M NaOAc electrolyte with 16 mM $NiSO_4$ (pH 5.3).

Figure 2.3. (a) Chronoamperograms and (b) mass change profiles of Au-coated quartz electrodes in 0.1 M NaOAc electrolyte with 16 mM $NiSO_4$ as a function of solution pH. Deposition in (b) was carried out at 1.35 V (vs. Ag/AgCl).

Figure 2.4. (a) Cyclic voltammograms of polycrystalline Au electrodes in 0.1 M NaOAc with 5 mM Fe(II) species (orange) and without Fe(II) species (black). All solution pH was adjusted to 5.3. (b) Mass change profiles of Au-coated quartz electrodes in 0.1 M NaOAc electrolyte with 5 mM $FeSO_4$ as a function of solution pH. Deposition was carried out at 1.05 V (vs.

Ag/AgCl).

Figure 2.5. (a) Cyclic voltammograms and (b) mass change profiles of 0.1 M NaOAc solution containing 5 mM $Fe_2(SO_4)_3$ (pH 5.3). Depositions in (b) were carried out at potentials denoted as dashed lines in (a).

Figure 2.6. Mass change profiles of 0.1 M NaOAc solution containing 16 mM $NiSO_4$ and $Fe_2(SO_4)_3$ as a function of the concentration of $Fe_2(SO_4)_3$ at 1.35 V (vs. Ag/AgCl). All solution pH was adjusted to 5.3.

Figure 2.7. Effects of different anions on the anodic deposition of nickel iron oxide. (a) Cyclic voltammograms and (d) mass change profiles of entry 1 (red), entry 2 (orange), and entry 3 (green) of Table 1. (b) Cyclic voltammograms and (e) mass change profiles of entry 1 (red), entry 4 (orange), and entry 5 of Table 1. (c) Cyclic voltammograms and (f) mass change profiles of entry 3 (green), entry 6 (orange), and entry 1 (red) of Table 1. All solutions possessed a pH of 5.3. The potentiostatic depositions in (d, e, f) were carried out at 1.35V vs. Ag/AgCl, denoted by the dashed lines in (a, b, c). M(II) represents 16 mM Ni(II) and 5 mM Fe(II) of metal salt precursors.

Figure 2.8. Proposed mechanism for the anodic deposition of NiFeOOH when (a) metal sulfate precursor and (b) metal acetate is used respectively.

Figure 2.9. Color of the deposition solution prepared by dissolving various metal-anion salts in electrolyte with different compositions. The top row shows the electrolyte composition of each column. The left column shows the metal salt composition of each row. pH was adjusted to about 5.3.

Figure 2.10. UV-Visible spectrum of aqueous solution of Fe salts in different anionic environment. Spectrum of just prepared solution and the solution after 1 hour of mixing was measured for (a) $FeSO_4$ in NaOAc and (b) $Fe(OAc)_2$ in Na_2SO_4 solutions.

Figure 2.11. (a) Cyclic voltammograms and (b) mass change profiles of $M(II)(OAc)_2$ in 0.2 M NaOAc (red), $M(II)(ClO_4)_2$ in 0.1 M NaOAc + 0.1 M $NaClO_4$, and $M(II)SO_4$ in 0.1 M NaOAc + 0.1 M Na_2SO_4. M(II) represents 16 mM Ni(II) and 5 mM Fe(II). All solution pH was adjusted to 5.3.

Figure 2.12. The effect of the total metal concentration in deposition solution on the growth of deposit. Deposition was carried out at 1.35 V (Ag/AgCl). All solution pH was adjusted to 5.3.

Figure 2.13. OER activities of NiFeOOH electrocatalysts with the loading mass of 0.2 μg cm^{-2} in 1 M KOH at the scan rate of 10 mV s^{-1}. The NiFeOOH electrocatalysts were deposited in the deposition baths with 0.1 M of Ni(II) and Fe(II) mixture with various molar ratios at 1.0 V (vs. Ag/AgCl).

Figure 2.14. (a) Cyclic voltammograms, (b) voltmassograms, and (c) mass change profiles of the Au-coated quartz electrodes under the previously reported deposition conditions (black) and the new deposition conditions (red). while the solution previously used for anodic deposition contained 16 mM $Ni(OAc)_2$ and 5 mM $Fe_2(SO_4)_3$ dissolved in 0.1 M NaOAc (pH 5.3). The dashed lines in the cyclic voltammograms and the voltamassograms denote the potentials where the potentiostatic deposition was carried out in the mass change-time plots.

Figure 2.15. (a) Top view and (b) cross-sectional FE-SEM images of the nickel iron oxide film deposited over 30 min on Au substrate. (c) Elemental line profiles along the cross section of the nickel iron oxide film deposited over 2 h on Au substrate by energy dispersive X-ray spectroscopy. (d) Thickness of the nickel iron oxide film as a function of the deposition time. The thicknesses of the nickel iron oxide film were measured using the cross-sectional FE-SEM images.

Figure 2.16. X-ray photoelectron core level spectra of (a) the Ni 2p region, (b) the Fe 2p region, and (c) the O 1s region for the nickel iron oxide film. (d) X-ray diffraction (XRD)

patterns of the nickel iron oxide film. The nickel iron oxide films were deposited over 30 min on the Au substrate.

Figure 2.17. Electrochemical performance of nickel iron oxide prepared by anodic deposition under the new condition. (a) Cyclic voltammograms of nickel iron oxide as a function of the deposition time (scan rate: 10 mV s^{-1}). (b) Tafel plot of the nickel iron oxide deposited over 2 h. (c) Comparison of catalytic the performance of the nickel iron oxide synthesized in this study with other NiFe-based electrocatalysts for the water oxidation reaction in terms of the overpotentials at 10 mA cm^{-2} and the Tafel slopes. (d) Chronopotentiometry result of nickel iron oxide at the constant current density of 10 mA cm^{-2} for 24 h.

Figure. 2.18. Photograph image of as-deposited NiFeOOH on the Au substrate under the new deposition condition.

Figure 2.19. (a) Overpotential of NiFeOOH required to reach the current density of 10 mA cm^{-2} and (b) Tafel slope with the deposition time.

List of Tables

Part 1.
Fabrication of Nanoporous Electrodes based on Self-assembled Indium Tin Oxide Nanocubes and the Geometric Effects on Electron transfer

1.1. Introduction

1.1.1. Nanoporous structures in electrocatalysts

Due to the aggravation of global crises such as severe climate change, recent pandemic and on-going wars, the globe is seeking to rapidly transition from the traditional fossil fuel-based industries towards greener and sustainable energy sources, and the associated energy generation and storage technologies. The governments from the developed parts of the globe led by the US and the European Union have recently announced foreseeable goals to achieve fully functioning hydrogen and biofuel economy.[2, 3] The race for cheaper and more efficient high performance electrocatalysts for various applications such as water electrolysis, energy storage devices, biomass and fuel cell technology has become more competitive than ever before, and it has developed into one of the main stream research themes for the science and engineering community.

For many decades, the main approach of developing better electrocatalysts undoubtedly has been to tailoring the catalyst composition and surface active sites in order to promote adsorption of the reactants and accelerate the catalytic processes.[4-9] In efforts to achieve this, the electrocatalysts were designed with various structures and compositions such as nanocasted 3D structures[10-15], core-shell nanoparticles[16-18], nanocages/nanoframes[12, 19, 20], heteroatom doped carbon-based structures[21, 22], and nanocomposite structures[23, 24] were fabricated.

Despite being developed independently, most of these electrocatalysts have distinct structural components with scales ranging from few nanometers to hundreds of nanometers. These ‘nanostructures’ are known to facilitate enlargement of active surface area and increase number of defects or active sites, which are tailored for better adsorption/desorption of reactants and products.[4-9]

The enlarged surface area is obviously beneficial to electrocatalysis. The electrochemistry involves electron transfer reaction between heterogenous phases, namely the solution and the solid electrode. The reactant has to come near the solid electrode in order for reaction to occur.

Due to this distinct nature, the place where the electron transfer, i.e. electrocatalysis, can occur is greatly limited to the surface area of the electrode in contact of the solution. Thus, we can easily envision that rough or porous electrodes with greater surface area can lead to enhanced catalytic activity than the flat electrode surfaces.

Meanwhile, the porous electrodes with rough surfaces contain various surfaces, which are susceptible to contact with the solution and can be electronically structured in such a way that adsorption or desorption of the catalytic species is promoted. Such structural effects were seen in many metal and metal oxide nanoparticles with controlled crystalline structures[25, 26], and porous carbon-based materials.[27]

The emergence of nanostructured electrocatalysts certainly elevated our knowledge on the inner workings of electrocatalysts and the associated electrochemical reactions. However, current mainstream research has become more and more material-oriented, active material through any exotic compositions with minimal control of crystalline facet and defects. Such indiscriminate search for any active materials quickly led to low repeatability, lack of scientific insight, excessive interpretation of results, which became a huge problem of understanding the true nature of electrocatalysts reported today, and many scientists are articulating the need for more standardized and well-thought experiments.[28-30] Despite the efforts in designing better electrocatalysts, the best performing benchmark material for major reactions still remains to be based on precious rare earth metal such as Pt, Pd, Rh, and Ir, or its derivatives.

1.1.2. Geometric effects of nanostructures

The major approach discussed in above section describes methodology for enhancing electrocatalysis that are based on the adsorption of the reactant materials. An alternate, less popular tactics in achieving higher catalytic activity via geometric effects were extensively researched by many groups including our group.[31-34]

Many researches have shown that the chemical reaction inside a confined space, such as

in charged microdroplets[35-38] and hollow nanoparticles[39-41] are highly accelerated when compared from that of the bulk. For instance, R. Zare et. al have reported synthesis of isoquinoline and substituted quinolines happening inside charged microdroplets generated by electrospray method, accelerated the reaction rate as much as 10^6 folds.[38] Such a large enhancement of these proton-catalyzed reactions was attributed to the combined effects of higher surface-to-volume ratio and proton concentrated at the microdroplet surface, where the reaction would take place. M. El Sayed et. al. experimented with five different hollow Pt, Pt/Pd, Pd nanocages with similar dimensions for reduction of 4-nitrophenol with sodium borohydride.[40] Due to the smooth surface morphology of the cube-shaped nanocages, defects and high-index crystalline facet was minimized. In their results, the material composing the inner surface of the nanocage was an important factor in determining the reaction rate of the catalysis reaction, showing that the reaction is heterogenous in nature, and the reaction takes place inside the nanocage rather than outer layers exposed to the bulk solution.

The reactant molecule situated inside a confined space are known to experience increased collision frequency with the electrode. H.S. White et. al., and R. J. White et. al. conducted a molecular dynamics study of the Brownian motion (or diffusion) of a reactant molecule and its interaction with the electrode.[42, 43] In a particular simulation, a reactant molecule in random motion can collide with the electrode 89 times while making 3 round trips from the solution surface to the electrode, suggesting that reactant molecule searches an area thoroughly before completely leaving the system. Because in an electrochemical reaction, many collisions are required for a reactant molecule to undergo electron transfer reaction, thus the reactant molecule in proximity to the electrode is more likely to react. Due to such nature of reactant molecules, confined spaces in nanoporous electrodes allow reactant molecules to encounter the electrode much often in a given time, greatly accelerating electrochemical reactions as a result.[31, 32, 44-46] Such increased collision frequency can give arise to catalysis of kinetically slow reactions such as oxygen reduction reaction, alcohol

oxidation and glucose oxidation.[31, 32, 45, 46]

The dielectric constant changes of solvent molecules inside a confined space were reported by many researchers.[47-50] For example, water confined inside nanopores are well known to display much lowered effective dielectric constant values.[50-52] Although the actual causes for this change are contested[53], it is generally known that the interaction between the water molecules and the nanopore interfaces and the subsequent alignment of other surrounding water molecules. The effective dielectric constant of water from these researches vary from $\epsilon_b \sim 80$ (bulk) to $\epsilon_b \sim 2$ (confined), meaning that water inside nanopores can be comparable to that of hydrophobic solvents and display completely different solvation behavior. Although not experimentally proven yet, the reactant molecules situated inside a nanopore can be highly destabilized due to the change in solvation and display completely different electrocatalytic behavior from when compared to that of bulk states.

The adsorptive behavior of the reactant inside nanopores is also susceptible to changes.[54-57] A computational study by P. Balbuena et. al. has shown that various calculated reaction parameters on Pt electrodes such as the adsorption energy, charge, bond length, and activation energy of the reactant were all influenced by the pore dimension where decrease in pore size generally lowered the activation energy and catalyzed the reaction.[55] Y. Liu et. al. observed pore-dependent changes in oxygen reduction reaction using N, O-codoped honeycomb-like carbon structure.[57] The carbon structure with the smallest, 12 nm pores displayed the best catalytic performance when compared to carbon with larger pores (22, 47, 60 nm), comparable to that of Pt/C catalysts. They attributed the enhanced performance to the decreased adsorption energy of O_2 molecules on the pyrindic active sites.

1.1.3. Nanoporous ITO electrode as an ideal model for observing geometric effects

The preceding researches on the structural effects of electrocatalysts mainly utilized catalytically active materials, such as Pt, Pd, alloys, or transition metal oxides. On the one

hand, this is useful for observing the combined impact that geometry can have on the material. However, many of these experimental designs are not optimal for observing the true effect of geometry. The active materials are designed to contain reactive centers, edge defects or crystalline facets, that could easily be changed with geometry. The result obtained by such structures would only exhibit the behavior that is dependent on the number of active sites available, which could be fine-tuned even without changing geometry. Furthermore, the active materials usually have highly adsorptive surfaces that are prone to fouling and unwanted side reactions. These can interfere with the target catalytic pathways and render inaccurate results. Lastly, the target catalytic reactions are usually proton coupled and multi-electron transfers, which can complicate and hinder correct interpretation of results.

Recently, our group have fabricated nanoporous electrodes by spin-coating commercially available ITO nanoparticles, and found that electron-transfer kinetics of $Fe^{2+/3+}$ ions was accelerated on the electrodes with thicker nanoporous layer even when the increased surface area was normalized.[44] In the research, ITO was deliberately selected as the catalyst material for observing the effects of pore geometry. ITO is a well-known electrochemically inert material, largely unaffected by the individual nanoparticle geometry, such as crystalline facet or defects. This property eliminated the possibility of large sample to sample variation in electrochemical reactivity, undesirable adsorption and side reactions. Thus, the accelerated catalytic properties displayed by the ITO nanoporous electrodes could solely be interpreted as the effect of nanoconfined space. Through structural engineering, it could be possible to tune the porous structures to further scrutinize the impact of geometry on electrocatalysts. Despite the qualitative findings, the ITO nanoporous electrodes still lacked well-ordered structures that are required to truely confirm and quantify the nanoconfinement effect to better understand the phenomenon. Besides, the thick randomly stacked nanoparticle layer of the electrode exhibited limitations in mass transfer.

1.1.4. ITO nanocube for nanoporous electrode material

Indium tin oxide or tin-doped indium oxide (ITO) is a representative transparent conductive oxide (TCO), mainly used in transparent display, photovoltaics, and conductive substrate material. This is due to its attractive properties such as optical transparency in visible light and good electrical conductivity, while being easy to prepare into films, easily patterned and chemically inert.[58, 59] In many electrochemical applications, especially biosensors, ITO is commonly used as a substrate material for anchoring biosensing catalyst and enzymes, and used to detect redox species such as H_2O_2 produced in the catalytic/enzymatic reactions.[59] In photovoltaics, ITO is also mainly used as a transparent substrate that is transparent to sunlight, while providing a robust electrical contact to the various dye materials in dye-sensitized solar cells (DSSC) and organic photovoltaics devices (OPV)[60, 61] Despite its advantages, the scope of applications in electrocatalysis using the ITO was very limited.

In the last decades, there were many attempts to fabricate nanostructured ITO for various applications. ITO/TiO_2 core-shell nanowire arrays for 3D substrate electrodes for DSSC were fabricated by H. Wang et. al., where ITO nanowire arrays were fabricated using polycarbonate template structures.[62] M. Davis et. al. fabricated 3D mesoporous ITO monolith by high temperature treatment of aerogel containing indium and tin precursors.[63] D. Fattakhova-Rohlfing et. al. synthesized well-ordered 3D mesoporous structures using block co-polymer (poly(ethylene-co-butylene)-b-poly(ethylene oxides) as a template [64]. Although these 3D-nanoporous ITO films have highly porous structures with some degree of order, complicated synthetic procedures and lacked large-scale uniformity. There also have been efforts to manufacture various colloidal ITO nanostructures, such as spherical nanoparticles[65-67] and nanocubes[68-71]. Among the various ITO-based nanostructures mentioned above, nanocubes displayed some noteworthy properties due to their highly crystalline structures and possibility for self-assembly. Ideally, the self-assembly of highly monodisperse, crystalline nanocubes could display large flat area of atomically defined crystalline facet as electrode surface and ordered geometric structures when assembled.

However, previously studied ITO nanocubes were highly polydisperse with varying sizes and morphology, and lacked any hint of self-assembly.

Meanwhile, semiconductor relative of ITO, indium oxide nanocrystals are usually known to be cubic nanostructures.[72-74] Unlike ITOs, research on indium oxides usually exhibited much more defined and monodisperse structures. Among them, X. Xu et. al. synthesized highly monodisperse, well-structured cubic indium oxide nanocubes, which caught our attention.[1] Through incorporation of tin to the structure via modification of synthetic procedures, we were able to synthesize monodisperse ITO nanocubes with truncated edges. Using these ITO nanocubes, hierarchical nanoporous electrode was fabricated by simple drop-casting and self-assembly of ITO nanocubes. By testing the electrochemical properties of the fabricated ITO nanoporous electrode, we could confirm the accelerated kinetics electro kinetics of ferric/ferrous ions and ascorbic acid by the geometric effect of nanostructured electrodes, while more complicated adsorptive electrochemical oxygen reduction reaction showed negligible geometric effect.

1.2. Experimental Section

1.2.1. Materials

Indium(III) chloride tetrahydrate (97%), tin(IV) chloride pentahydrate (98%), oleylamine (tech. grade, 70%), ethanolamine, potassium hexacyanoferrate (II) trihydrate, hexaammineruthenium (II) chloride, iron(II) sulfate heptahydrate, iron(III) sulfate heptahydrate, L-ascorbic acid, sodium sulfate, sodium perchlorate were all purchased from Aldrich. Absolute ethanol (Emsure ACS, ISO, Reag. Ph Eur) was purchased from Merck Millipore. Sulfuric acid (95%), cyclohexane (99.5%), isopropanol (99.5%) were obtained from Daejung Chemicals (Korea). Deionized water used in experiments were prepared with Thermo Scientific Barnstead Nanopure Ultrapure water system (Resistivity of ~18 MΩ). ITO glass was obtained from Techinstro.

1.2.2. Synthesis of ITO nanocube

ITO nanocube was synthesized by modifying experimental method for preparing uniform cubic indium oxide nanocubes developed by X. Xu et. al.[1] In a typical synthesis, 407 μmol of indium(III) chloride tetrahydrate and 20.3 μmol of tin(IV) chloride pentahydrate were dissolved into a mixture of 11.94 mL absolute ethanol and 7.5 mL oleylamine. When fully dissolved, 60 μL of deionized water was carefully added to the above mixture dropwise while in sonication. Without sonication, the mixture sometimes forms insoluble white fibril-like structures, which hampers the formation of the nanocube. Upon addition of water, the mixture becomes slightly opaque due to emulsion formation. The mixture is then transferred into a 50mL Teflon-lined hydrothermal reactor and heated to 240 °C for 24 h in an oven. Then the reactor was left to cool to room temperature. After cooling, the mixture was initially centrifuged at 5000 rpm for 5 min and redispersed three times in cyclohexane to remove any small premature particulates and reactants. The resulting precipitate was then centrifuged and redispersed via sonication in a mixture of isopropanol and ethanolamine (9:1 in volume) three times for ligand exchange. After the ligand exchange, the precipitate becomes readily dispersible in hydrophilic solvents such as isopropanol and ethanol. The precipitate was then dried in a vacuum oven, and stored in a powdered form for later use.

1.2.3. Preparation of self-assembled nanoporous ITO nanocube electrode

For preparing a self-assembled nanoporous ITO nanocube electrode, ITO glass was used as the substrate electrode. The ITO glass was first washed and sonicated consecutively in acetone, isopropanol and water to remove any dusts and residues. Then the ITO glass was electrically contacted using an aluminum conductive tape near the edge of the ITO glass. Kapton tape was used to protect the contact, and electroplating tape (3M™ Electroplating Tape 470) with 6 mm diameter hole was used to selectively expose an area. A desired amount

of ITO nanocube was thoroughly dispersed in a 1:1 mixture of isopropanol and deionized water via sonication. The mixture was then drop-casted onto an ITO glass. Due to the nature of cubic colloids[75], the ITO nanocubes self-assembled into cubic clusters without any additional treatment. The drop-casted glass was dried at ambient temperature and pressure. The prepared electrode was then carefully rinsed with deionized water before electrochemical experiments.

1.2.4. Electrochemical measurements

All the electrochemical experiments were done in a three-electrode system using either a Hg/Hg_2SO_4 (MSE; saturated K_2SO_4, RE-2C, BAS, Inc.) or Ag/AgCl (3M NaCl, self-made) as a reference electrode. Coiled Pt-wire was used as a counter electrode. The cyclic voltammetry (CV) and linear sweep voltammetry (LSV) was performed using CHI660A electrochemical workstation (CH Instruments, Inc., USA). The electrochemical impedance spectroscopy (EIS) was conducted using Reference 600 (Gamry Insturments, Inc., USA). Data of the EIS experiments were fitted by using the simplex method in the Gamry Echem Analyst software.

1.2.5. Characterization

TEM images were obtained using Hitachi H-7600 electron microscope. SEM images were obtained using Hitachi Su-70 field emission scanning electron microscope. XRD measurements were obtained with Bruker D8-Advance X-ray diffractometer at the Research Institute of Advanced Materials.

1.3. Results and Discussion

1.3.1. Synthesis and characterization of ITO nanocube

The synthesis method (Figure 1.1A) used in this article is modified from previously

investigated method by X. Xu et. al. [1], which was used to synthesize highly monodisperse cubic indium oxide (c-In_2O_3) nanocubes with truncated edges. Although the synthesis of c-In_2O_3 nanocubes could be replicated (Figure 1.2A), a simple addition of tin precursor to the synthetic mixture discussed by X. Xu et al resulted in irregularly shaped nanoparticles (Figure 1.2B), thus a modification of the synthesis method is necessary. We found that higher synthesis temperature, addition of minute amount of water, and usage of specific ethanol as a reagent was essential in order to properly incorporate tin into the indium oxide. With some modifications, ITO nanocubes of similar dimensions to the In_2O_3 nanocubes could be produced, accompanying a color change from white to sky-blue as described in Figure 1.1B, C and respective insets. With further optimization, large scale self-assembly of nanocubes were observed on simply dried TEM samples (Figure 1.1D).

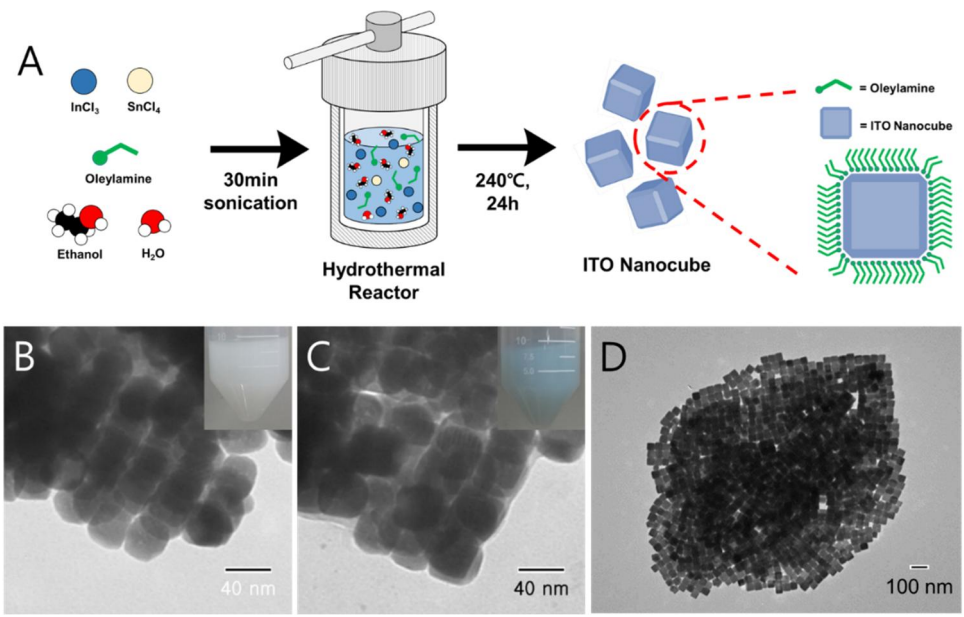

Figure 1.1 (A) A general scheme describing synthesis of ITO nanocubes. As-prepared ITO nanocubes are ligated with oleylamine. TEM images of (B) In_2O_3 nanocubes prepared with method by X. Xu et. al.[1] and (C) ITO nanocubes prepared with modified procedures to incorporate Sn into In_2O_3. The insets in B and C are photos of solutions of respective nanocubes. (D) A low magnification TEM image of ITO nanocubes and its self-assembly

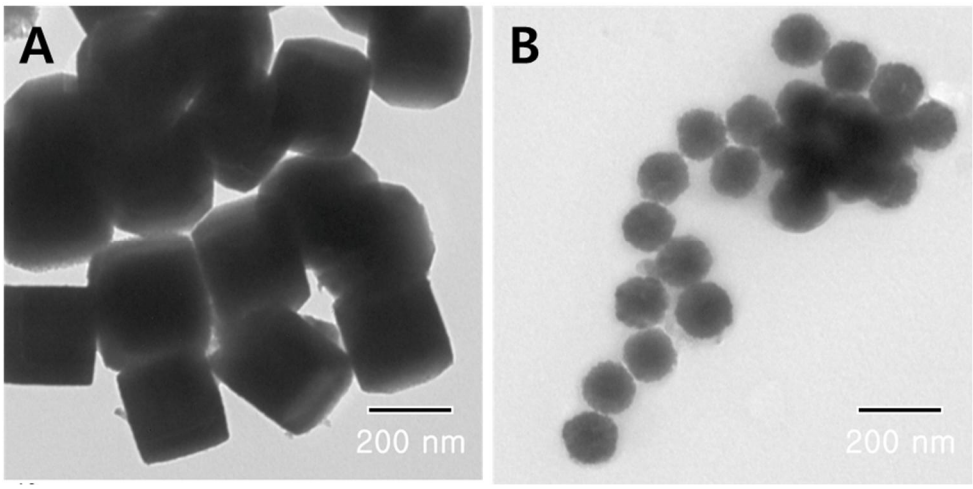

Figure 1.15 (A) TEM images of indium oxide synthesized using the previous method and (B) the result when tin precursor was simply added to the reaction mixture used to synthesize indium oxide in (A)

Figure 1.3 describes the effect of temperature on the morphology of indium oxide and ITO. The synthesis temperature described in previous method is 225°C, and the various effects described was replicable (Figure 1.3A~F). At low temperatures, the InOOH nanorods were synthesized and as the temperature rose, the InOOH nanorods started to aggregate into small bundles and became nanocubes when the temperature was raised above 220°C. When tin was added, the synthesis temperature had to be raised to at least 240°C required to become nanocubes as can be seen in Figure 1.3F. Incorporation of tin generally decreased the size of the nanocubes from 50~60 nm to 40 nm, which can be seen in Figure 1.3G~I, and changed the color of the product from pure white to sky-blue. Figure 1.4 shows XRD diffractogram of ITO nanoparticles synthesized under various temperatures. As the temperature was raised from 160°C to 200°C, the strong peak around 31° starts to be visible. Above 220°C, fully crystalline peaks corresponding to c-In_2O_3 could be observed. No peaks corresponding to SnO_2 was observed, which is similar to other previous reports.[76-78]

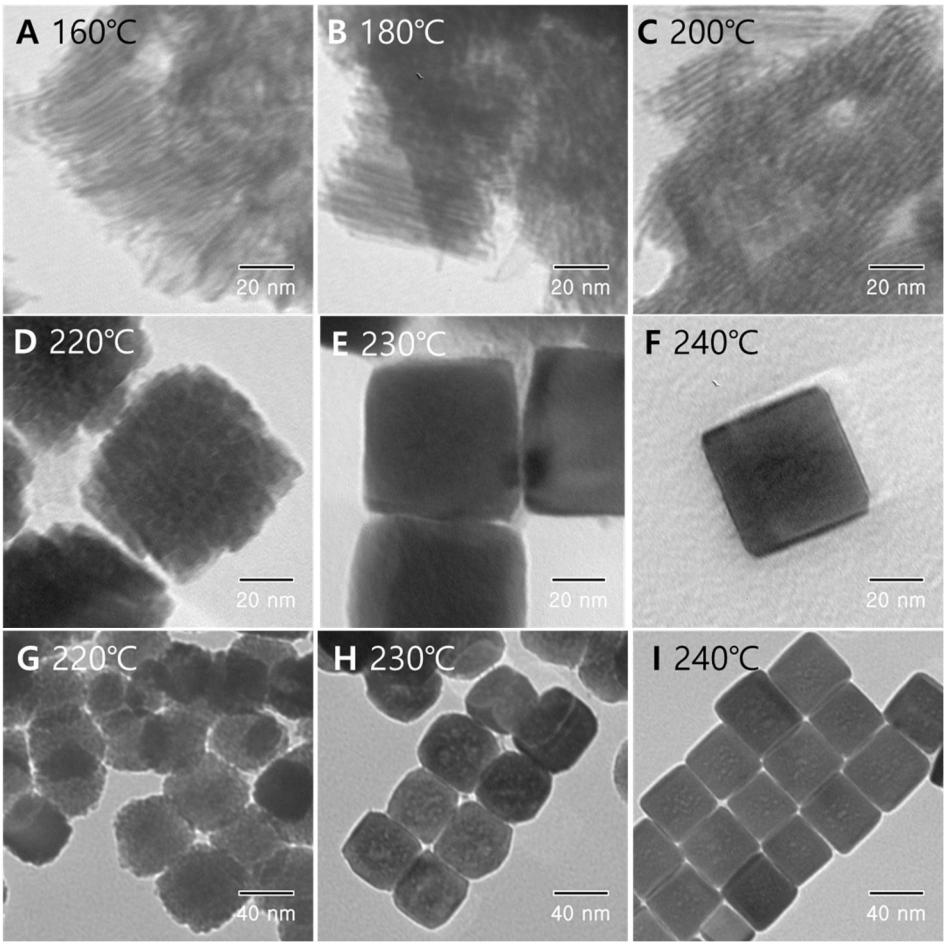

Figure 1.16 TEM images of indium oxide (A to F) and indium tin oxide (G to I) synthesized at different temperatures labelled on the image.

Figure 1.5 shows TEM and SEM images of the ITO nanoparticles synthesized with different water content. According to the TEM images, a small amount of water is required to form various shapes with defined edges. With very little to no water in the system, the nanoparticles assumed largely spherical shapes, but with irregular jagged surfaces. At 1.0% water content, the resultant particles were truncated nanocubes with sizes around 100 nm. Higher water content resulted in larger-sized mixture of cubic and hexagonal shapes, which could not be separated with simple centrifugation. Figure 1.5F and g show the SEM images of particles synthesized with 1.0% and 1.5% of water. From Figure 1.5F, the truncated edges of the nanocube could clearly be seen. From Figure 1.5G the various shapes seen in the TEM

images are different projections of cuboctahedrons, which could be a square, a regular hexagon and slightly deformed hexagons. The change in shapes from a truncated nanocube to a cuboctahedron indicate that water in the reaction mixture influences growth speed of certain particular crystalline facet. Although the cause of this preferential growth is uncertain, we suspect that the water in the system could react with oleylamine to produce positively charged oleylammonium ion, which could stabilize certain facets differently. Despite this finding, the degree of truncation in the ITO cubes at high water content could not be controlled in a reproducible way. Thus, we have decided against testing the ITO cuboctahedrons in later electrochemical studies.

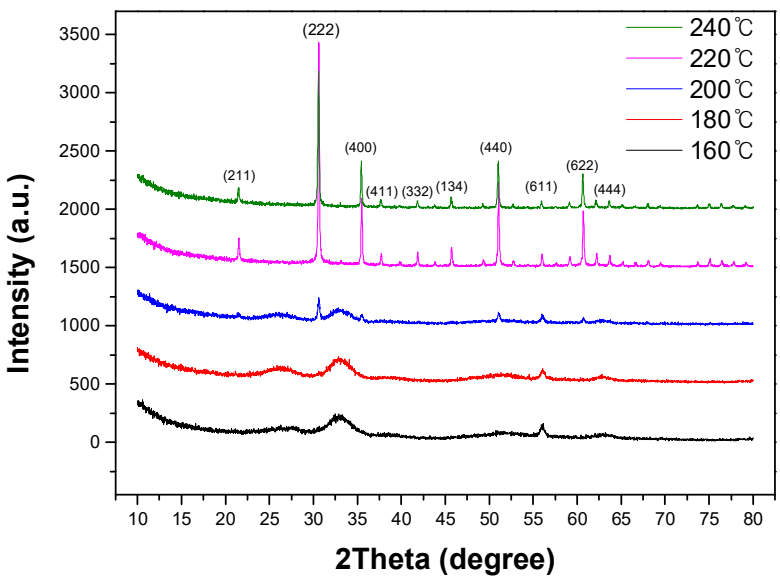

Figure 1.4 XRD diffractogram of ITO nanoparticle synthesized under various temperatures.

Figure 1.6 depicts the effect of ethanol received from various manufacturers on the morphology of the synthesized ITO. Despite requiring addition of about 1% of water in volume against ethanol, the morphology of the ITO was independent of the natural water content of the ethanol used. Rather, cube-shaped ITO could only be synthesized using Merck Millipore's 99.9% purity absolute ethanol (EMSURE). High purity (>95.6%) ethanol is

known to contain trace amount of separation agents such as benzene or pyridine, and may differ from product to product. We suspect that presence of these trace organic compounds could be critical factor in determining the shape of the ITO products.

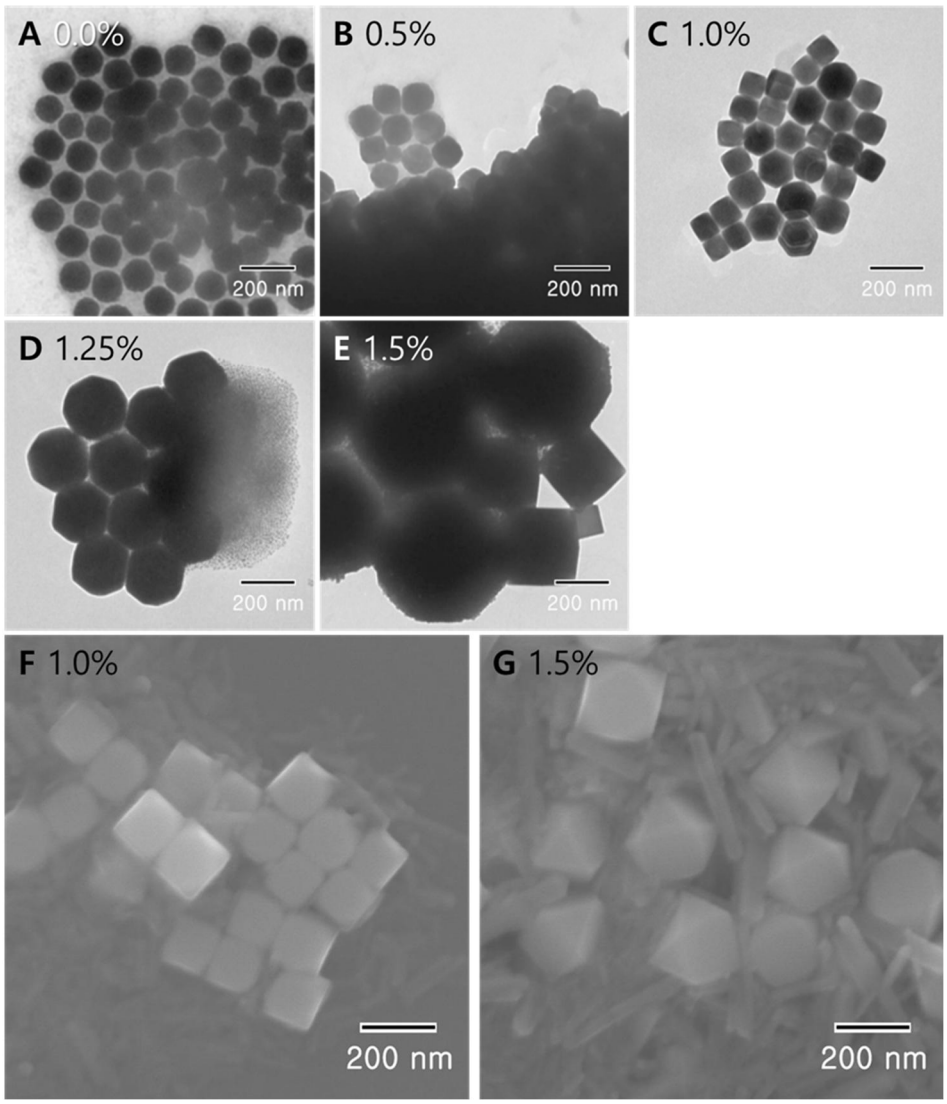

Figure 1.517 TEM images (A to E) of ITO synthesized by varying water content in the precursor solution. Figure F and G shows SEM images of ITO synthesized with 1.0% and 1.5% water content respectively. The percentage described in the figure is volumetric percentage of ethanol and water. For example, condition in figure b is 99.5% ethanol and 0.5% water by volume.

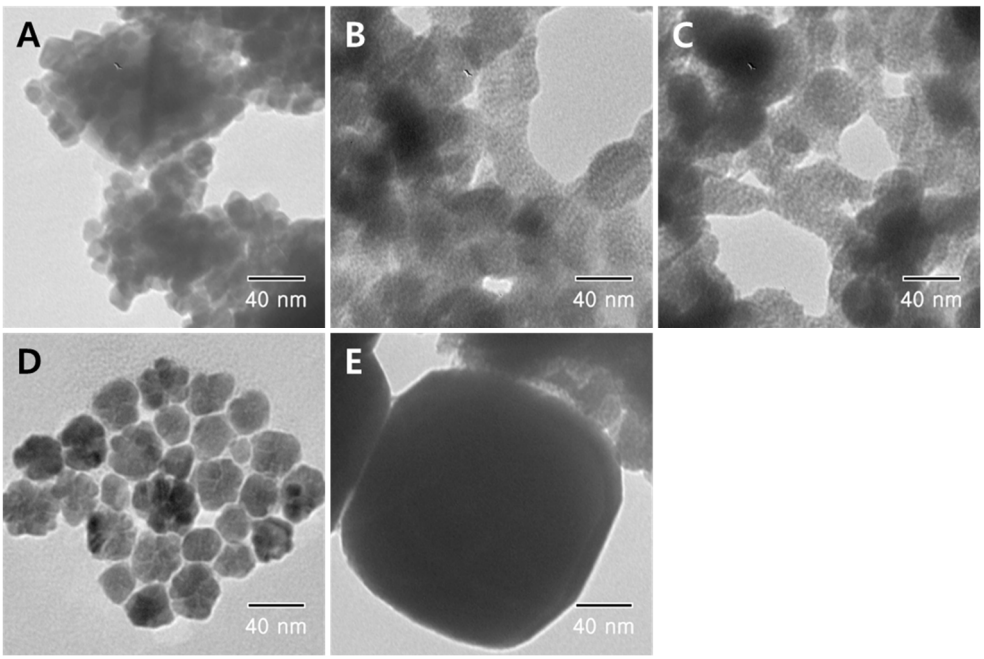

Figure 1.6 TEM images of ITO synthesized using various commercially-available ethanol products; (A) Daejung Chemical 94.5% purity ethanol, (B) Daejung Chemical 99.9% purity absolute ethanol, (C) Aldrich 99.5% purity ethanol, (D) – Aldrich 99.8% purity absolute ethanol (GC), (E) – Merck Millipore 99.9% purity absolute ethanol (EMSURE ACS, ISO, Reag. Ph Eur)

1.3.2. ITO nanocube self-assembly and fabrication of nanoporous electrodes

Figure 1.7 describes overall scheme of fabrication of nanoporous ITO nanocube electrode. As we can see in the figure, as-prepared ITO nanocube is hydrophobic due oleylamine, which acts as a ligand. Hydrophobic ligand on the surface could obstruct electrical contact between the ITO substrate and ITO nanocubes, and may hamper interactions with the solution used in electrochemical experiments. Hence, the ligand was exchanged from oleylamine to ethanolamine using repeated dispersion in excess ethanolamine, sonication, and centrifugation. After the ligand exchange, the nanocube became readily dispersible in hydrophilic alcohols such as isopropanol and partially stable in deionized water. No change

in the morphology was observed after the ligand exchange.

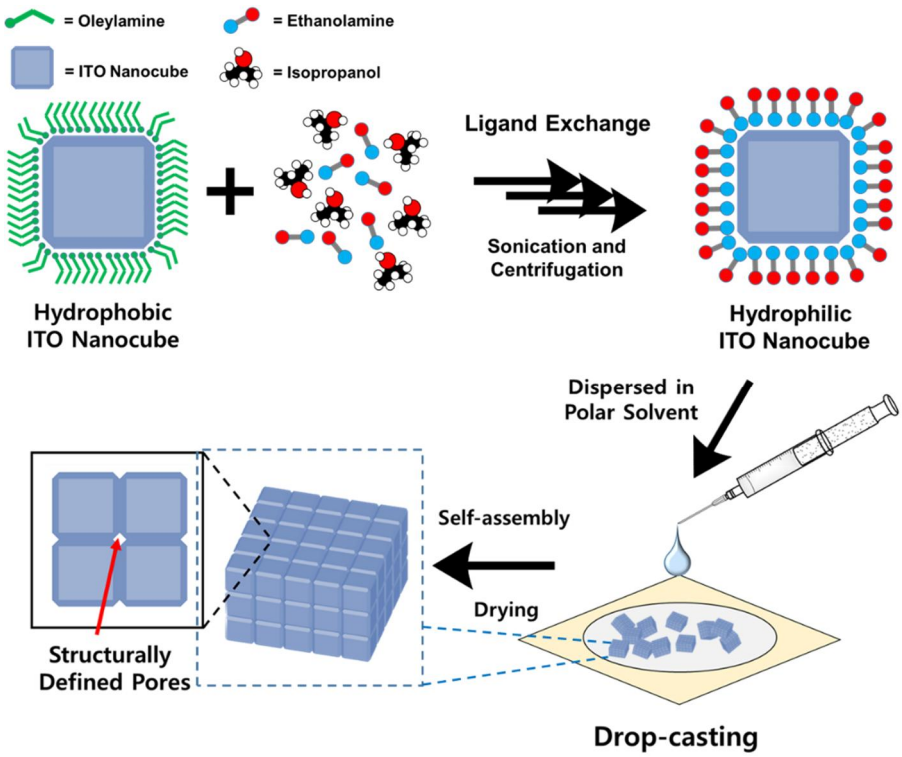

Figure 1.7 Overall scheme of ITO nanocube post-treatment and fabrication of nanoporous ITO nanocube electrode.

The nanoporous ITO nanocube electrode was synthesized by drop-casting method.[79] High temperature treatment was not conducted due to the slight morphological deformation of ITO nanocube (Figure 1.8).

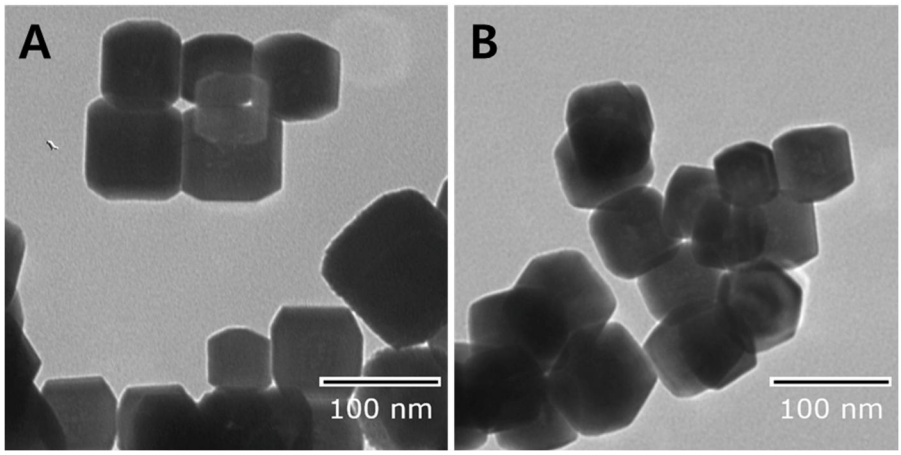

Figure 1.8 TEM images of morphological change in ITO nanocubes (A) before heat treatment and (B) after heat treatment. Slight change in nanocube morphology and size was observed as a result of heat treatment

The ligand exchanged ITO nanocube is partially dispersible in water, and tend to aggregate into clumps. In order to prevent large particulates from forming, 1:1 mixture of isopropanol and deionized water was used for electrode fabrication. Cube-shaped nanoparticles are known to self-assemble into bigger cube-shaped aggregate due to van der Waal's interaction between the large flat surface of the cubes.[75] As can be seen in Figure 1.9A and B, ITO nanocubes naturally self-assembled into small cube-shaped clusters. Because of the truncated nature of the synthesized nanocubes, the self-assembly of nanocubes creates small pores between the edges as depicted in the scheme in Figure 1.7 and TEM image in Figure 1.9C. Such pores are smaller than 10 nm in size and 80 nm deep, and likely to be three dimensionally interconnected. Furthermore, the surface created by truncations is likely composed of defined crystalline facet, which is unseen in commercially available ITO nanoparticles. These properties of the self-assembled ITO nanocube is highly advantageous because all the pores are of same dimension and similar in electrochemical reactivity.

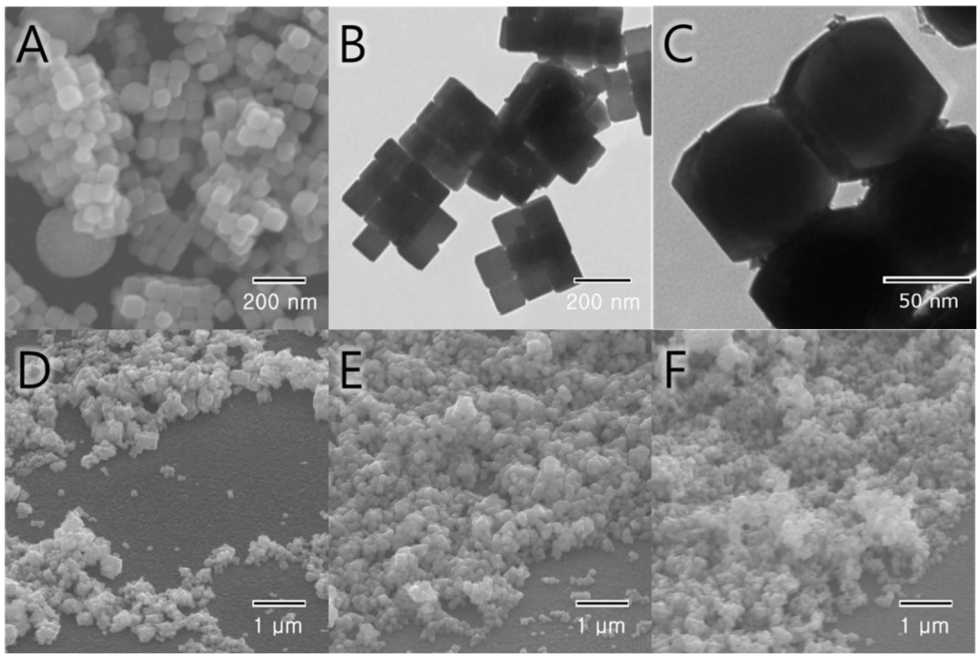

Figure 1.9 (A) SEM and (B) TEM images of ITO nanocube used for electrochemical studies. (C) A higher magnification TEM image of self-assembled ITO nanocubes, showing structurally defined pore created by self-assembly. (D~F) SEM images of self-assembled ITO nanocube electrode, which (D) 20 μg, (E) 50 μg and (F) 100 μg of ITO nanocube was drop-casted onto ITO glass substrate.

The size and shape of the self-assembled nanocube clusters, however, was incontrollable. This could be due to inhomogeneity in ITO nanocube morphology such as size and shape. In Figure 1.9D to F, the electrode created with the nanocube is composed of random aggregation of the small self-assembled clusters. Although this might not be an ideal self-assembled electrode, loose aggregation of small clusters created multi-modal structure, which could be advantageous for mass transfer of reactants to the electrode. As the nanoparticle loading increased from 20 μg to 100 μg, uncovered ITO glass substrate decreased, eventually covering the whole surface. Unlike spin-coating utilized in our previous study using commercially available ITO nanoparticles[44], thickness of the ITO aggregates could not be determined precisely, because of the large variation in coverage, where clear distinction of exposed ITO glass substrate surface and nanocube agglomeration can be made.

1.3.3. Fundamental electrochemical behavior at nanoporous ITO nanocube electrodes

In order to test the usability of the prepared nanoporous nanocube electrode, it was first tested in blank electrolyte solution. Figure 1.10A shows increase in charging current with ITO nanocube loading due to enlarged surface area, compared with that of bare ITO. Figure 1.10B also shows linear current-scan rate relationship indicating good capacitive behavior. The capacitances obtained from slope of Figure 1.10B were used to calculate electrochemical surface area (ECSA) for all the electrodes and it is summarized in Table 1.1. With 100 μg loading, the relative ECSA is calculated to be about 18 times larger than that of the bare ITO glass substrate. The 18-fold increase in area appears to be lower than expected in Figure 10F. This is because the side surfaces of the nanocube are in contact with each other by self-assembly, so the empty space created is relatively small. The nanoporous ITO nanocube electrodes were then tested with reversible redox species such as $Ru(NH_3)_6^{2+}$ and $Fe(CN)_6^{2+}$. Figures 1.10C and D shows the cyclic voltammograms of these redox species on the electrodes with varying ITO loading. Compared with the bare ITO electrode, there is little difference in the shape of cyclic voltammograms of the nanoporous electrodes because the reaction of the reactant is fast enough that it cannot enter the nanopore. The peak-to-peak potential separation is also virtually unchanged and cyclic voltammograms are not inclined, indicating good conductivity of the nanoporous electrodes.

Table 1.3 Electrochemical capacitance and relative electrochemical surface area calculated from Figure 1.10B

Electrode	Average C_{dl} (nF cm^{-2})	Ratio	Relative Electrochemical Surface Area (cm^2)
Bare ITO	13.91	1.00	0.283
ITO 20 μg	36.65	2.64	0.745
ITO 50 μg	125.24	9.01	2.546
ITO 100 μg	254.97	18.34	5.184

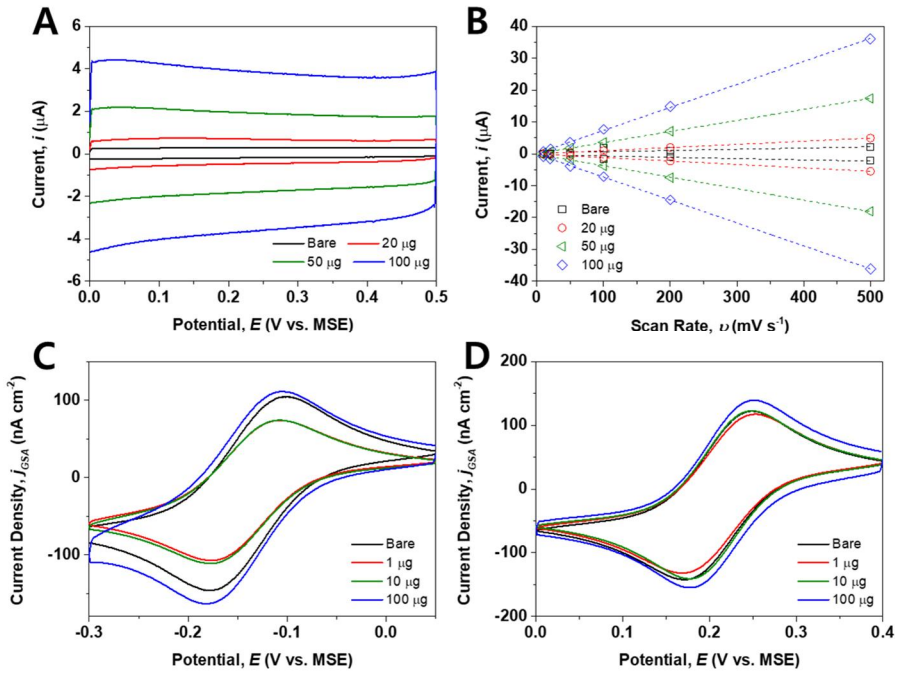

Figure 1.10 (A) Cyclic voltammograms at bare ITO electrode and nanoporous ITO nanocube electrodes with different ITO loading in 0.1 M Na_2SO_4 (pH 7) solution and (B) Relationship between current density and scan rate obtained from data of (A). Cyclic voltammogram of (C) 1 mM $Ru(NH_3)_6^{2+}$ and (D) 1mM $Fe(CN)_6^{2+}$ in 0.1 M Na_2SO_4 (pH 7) solution. The current in these voltammograms is normalized by the geometric surface area (GSA). Scan rate = 50 mVs^{-1}.

The $Fe^{2+/3+}$ redox reaction was chosen as a model electrochemical reaction for probing electron-transfer kinetics at nanoporous ITO electrodes. This redox reaction is well-studied outer-sphere reaction that involves simple single electron transfer without any side reactions. Also, it is known to have substantial reorganization of primary solvent shell upon redox reaction[80], and is slow enough to observe changes in reactivity on electrochemically inert electrodes, which is ideal for our purpose of observing effect caused by the nanoporous structure.

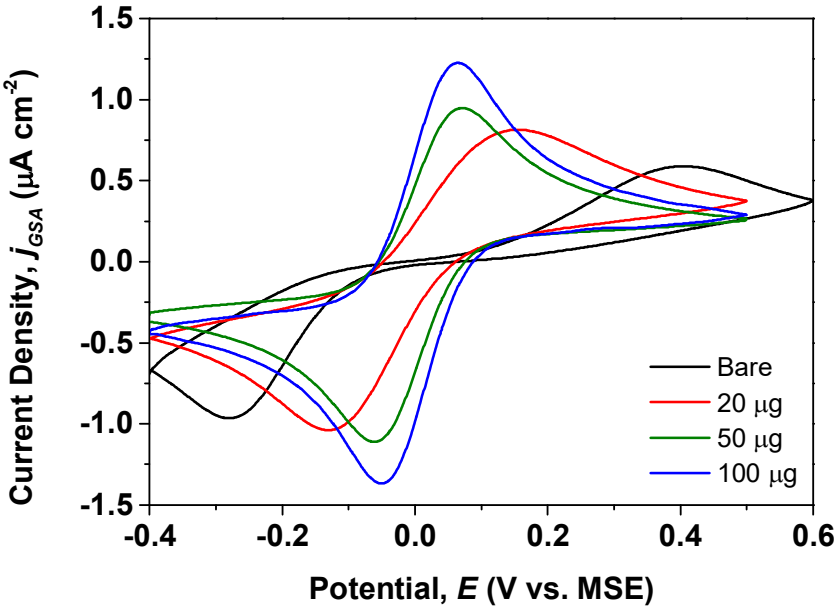

Figure 1.11. Cyclic voltammograms of $Fe^{2+/3+}$ in 0.1 M H_2SO_4 and 0.1 M Na_2SO_4 solution on ITO nanocube electrodes. The current density was normalized with GSA. Scan rate = 50 mV s^{-1}.

The cyclic voltammograms in Figure 1.11 show $Fe^{2+/3+}$ redox reaction on bare and nanoporous ITO electrodes with different nanocube loadings. Separation distance between the anodic and cathodic peak potentials is wide at bare electrode because the catalytic activity of the ITO electrode is very low. It shows that higher nanocube loading results in closer peak-to-peak separation. In general, a narrowing of the peak-to-peak separation means that the reactivity of the electrode is improved. In other words, this implies that the electron-transfer process is much faster at higher nanocube loadings. This result is in correspondence with our previous study done using electrodes fabricated with commercially available ITO nanoparticles[44], where thicker porous ITO layer showed closer peak-to-peak separation.

We further analyzed the nanoporous nanocube electrodes with electrochemical impedance spectroscopy (EIS) because narrowing of peak-to-peak separation can be reduced by limitation of mass transport of the reactants as well as enhancement of the reactivity in the

porous electrode.[81] Impedance results were fitted based on Randles equivalent circuit[82] in Figure 1.12 D, with capacitive component being replaced by a constant phase element (CPE). This accounts for the non-ideal capacitance behaviors typically seen in electrodes with rough or porous surface.[83-85] Figures 1.12 A and B shows the Nyquist plots of $Fe^{2+/3+}$ redox system on the ITO nanocube electrodes, where the impedance was normalized with GSA of the electrode used. The semicircle on the bare ITO glass electrode was very large barely reaching the Warburg region, while the nanoporous ITO electrodes clearly showed much smaller semicircle with higher loading. This corresponds to smaller charge transfer resistance (R_{ct}), which is usually a good indicator of faster electron-transfer, thus higher electrode kinetics.[86] Even when impedances were normalized with ECSA calculated in Table 1.1, the nanoporous ITO electrode with higher loading showed smaller R_{ct} as shown in Figure 1.6 C. The solution resistance (R_s) appears to increase, which is an artifact from normalizing with the ECSA. The R_s depends on the GSA, and the GSA is constant even though the ECSA increases in a nanoporous electrode. In fact, when the R_s is obtained without area correction, there is no difference in resistance (Table 1.2).

The EIS fitting data was used to calculate the standard rate constant (k^0) using relations derived from Nernst equation and current-overpotential equation.[82]

$$k^0 = i_0/FAC \tag{1}$$

$$i_0 = RT/FR_{ct} \tag{2}$$

where i_0 is the exchange current, F is the Faraday constant in C, A is the electrode surface area, C is the concentration of reactant, R is gas constant, and T is temperature in Kelvin. The ECSA calculated in Table 1.1 was used for the electrode surface area calculation. The result is summarized in Table 1.2.

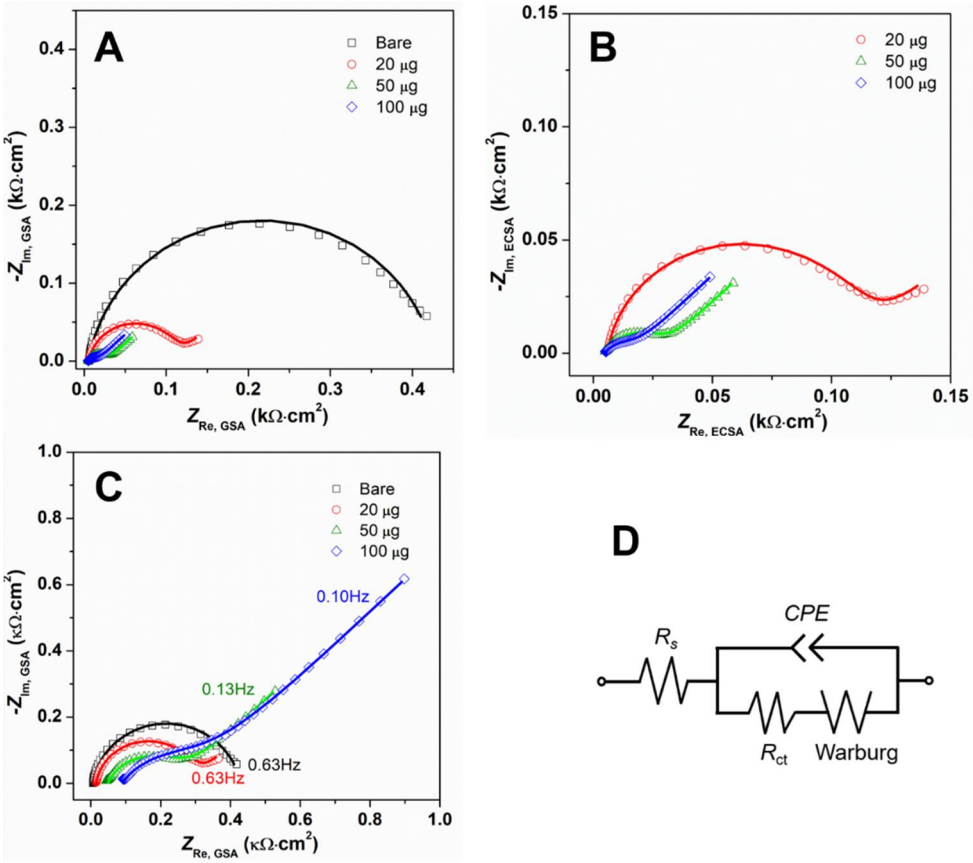

Figure 1.12 (A) Nyquist plots of $Fe^{2+/3+}$ redox system on the bare and nanoporous ITO electrodes. (B) Zoomed in view of the Nyquist plot (A) for better comparison of nanoporous nanocube electrodes with different loadings. The impedance in (A) and (B) was normalized with geometric surface area (GSA). (C) Nyquist plot of $Fe^{2+/3+}$ redox system on the ITO nanocube electrodes normalized with electrochemical surface area (ECSA). (D) Randles circuit that was used to fit the EIS data.

Table 1.4 Values obtained from the fitting process for bare and nanoporous ITO shown in Figure 1.12.

Electrode	R_s (Ω)	R_{ct} (kΩ)	$R_{ct, GSA}$ (kΩ·cm²)	$R_{ct, ECSA}$ (kΩ·cm²)	k^0 (cm/s)

Bare ITO	19.1	1.49	0.42	0.42	6.31×10^{-5}
ITO 20 μg	19.8	0.38	0.11	0.28	9.51×10^{-5}
ITO 50 μg	17.1	0.089	0.025	0.23	1.17×10^{-4}
ITO 100 μg	17.3	0.053	0.015	0.28	9.67×10^{-5}

The k^0 value calculated using the EIS data clearly shows that the redox reaction of $Fe^{2+/3+}$ is enhanced at the nanoporous ITO nanocube. Flat bare ITO glass had the smallest value of 6.31 x 10^{-5} cm s^{-1}, while the ITO nanocube electrode with 50 μg loading had the highest k^0 with value of 1.17 x 10^{-4} cm s^{-1}, almost two times higher than the flat counterpart. Considering that the same nanocube was drop-casted onto the electrode, we can expect the roughly same degree of nanoporous structure on each self-assembled ITO nanoncube cluster, composed of ITO nanocubes with defined crystalline structure and facets, minimizing any variations in the reactivity of different pores. We also can exclude effect of the enlarged surface area due to normalization of ECSA to raw data. Thus, we conclude that nanoporous structure created by the self-assembly of ITO nanocubes are the main origin for this catalytic enhancement, with minimal contributions of any defects acting as active sites, confirming nanoconfinement effect.[44, 45] Accepting higher reactivity in nanoconfined space, we should expect increased k^0 with higher loading, which would create more confined space. However, electrode with 50 μg loading had the highest while electrode with 100 μg loading had slightly lower k^0 value. It seems that the increased electrode area of the nanoporous layer is not fully used for the reaction of the reactants due to limitation of mass transport into nanopores.

When compared to the k^0 values from the previous study using nanoporous electrode fabricated with commercially available ITO nanoparticles[44], the ITO nanocube electrodes displayed superior activity. The k^0 value from the previous work was around 1.5 x 10^{-5} cm s^{-1}, whereas the k^0 value from the self-assembled ITO nanocube electrode was about 1.0 x 10^{-4} cm s^{-1}, almost 7 times higher although smaller amount of ITO material was used to fabricate the electrode. This augmented k^0 value may be attributable to the high crystallinity of the ITO

nanocubes, better conductivity, smaller pore dimensions and better uniformity of electrode surface.

1.3.4. More complex reactions at nanoporous ITO nanocube electrodes

From the last section, we explored the effects of nanoporous structure on a simple reaction involving single electron transfer and non-adsorptive mechanism. In order to further enlighten our understanding of geometric effects, more complex reactions with multi-electron, inner sphere reactions were considered.

Ascorbic acid is an important metabolite with pro- and anti-oxidative properties, which is one of common target biomolecules in biosensors. The usual way of detecting ascorbic acid is by electrooxidation, which occurs at about +0.6 V on Pt, and +0.4 V on glassy carbon electrodes. The oxidation involves one or two electrons and protons depending on the chemical environment.[87, 88] At physiological pH condition around pH 7, single irreversible oxidation peak is observed at most electrodes.

Figure 1.13 shows CV and EIS results of ascorbic acid oxidation at pH 7. From the cyclic voltammograms, the oxidation peak potential is negatively shifted with the increased ITO nanocube loading. This can be interpreted as increased reactivity, as in $Fe^{2+/3+}$ redox system, aside from a minor difference that the oxidation reaction was irreversible. K. Nam et. al. reported that ascorbic acid oxidation on microporous carbon electrodes reversible behavior.[89] Such reversibility was not observed on nanoporous ITO electrodes. In Figure 1.13C, the oxidation peak current was normalized to 1 in order to better distinguish the onset potential at each nanocube loadings. The order of onset potential was observed to be 100 μg < 20 μg < 50 μg < bare ITO electrode, which was different from the $Fe^{2+/3+}$ redox system. Naturally, one would expect nanoporous electrode with higher loading to be more electrochemically catalytic, but this was not the case for ascorbic acid oxidation observed in this set of experiments. Moreover, the EIS results in Figure 1.13D and the calculated k^0 value in Table 1.3 further complicated the issue, as the order of onset potentials and k^0 value did

not match accordingly. The 20 μg loading had the highest k^0 while the 100 μg loading had the lowest, but all they were mostly very close in value. This result suggests that there was very little geometric effect of the porous electrode for ascorbic acid oxidation.

The known electrochemical oxidation mechanism of ascorbic acid involves adsorption of hydroxide functionalities onto the electrode.[90] Additionally ascorbic acid is known for its adsorptive capabilities on various electrode materials, such as transition metals as well as commonly used glassy carbon (GC), Pt and Au electrodes.[90] On Pt electrode, for example, when it was dipped in the ascorbic acid solution for about 3 minutes without any stirring was reported to be covered almost completely with adsorbed ascorbic acid.[91] On carbon-based electrodes, it was reported that adsorption and catalysis of ascorbic acid species were highly dependent on the surface functionalities of the electrode, and various effects and activity of different functionalities still remains elusive.[92]

Despite the large porous electrode surfaces generated by the self-assembled ITO nanoncubes, the material was ineffective in facilitating electrocatalysis through the aforementioned geometric effects of nanoporous electrodes. Because ITO is a well-known electrochemically inert material, the adsorption of ascorbic acid would have been difficult, which is a crucial step of ascorbic acid electrooxidation. This suggests that unlike the outer sphere electron transfer reactions such as $Fe^{2+/3+}$, the inner sphere ascorbic acid oxidation is electrode material-dependent and requires active electrode surface rather than large inactive surfaces. Notwithstanding rather disappointing results, the nanoporous ITO nanocube electrode still produced electrocatalytic electrodes with more negative onset potential when compared to the bare electrode, which could be an important aspect to consider when designing electrocatalysts in sensor applications.

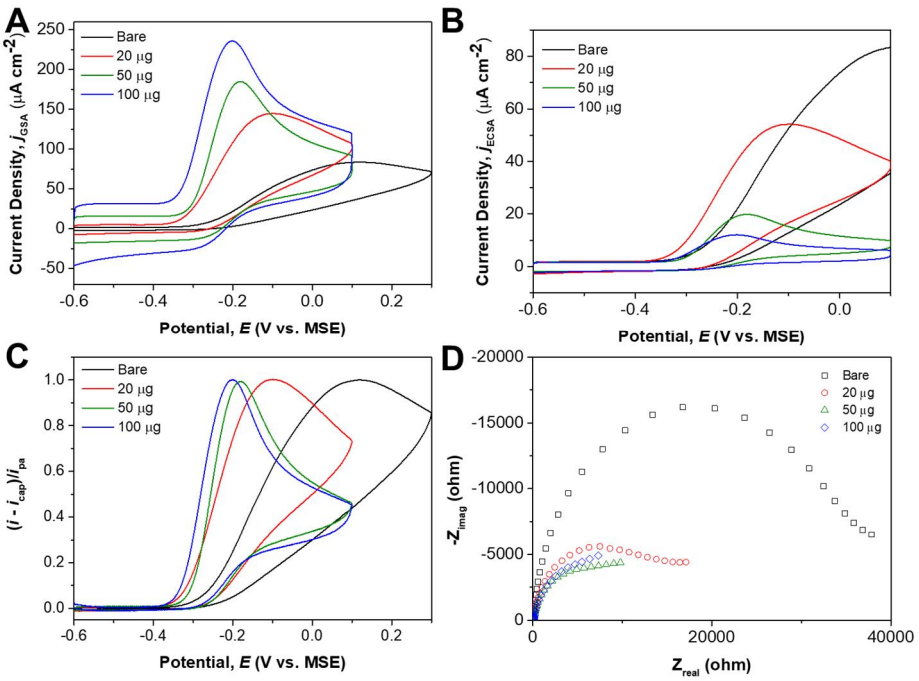

Figure 1.13 Cyclic voltammogram of 1 mM ascorbic acid in 0.1 M $NaClO_4$ at pH 7 on bare and nanoporous ITO electrodes, which the current was normalized with (A) GSA and (B) ESCA. (C) Cyclic voltammogram where anodic peak current was subtracted by respective capacitive current, then normalized to 1. (D) Nyquist plot for ascorbic acid oxidation on bare and nanoporous ITO electrodes.

Table 1.3 Values obtained from fitting ascorbic acid oxidation results from Figure 1.13.

Electrode	R_{ct} (kΩ)	$R_{ct,\ GSA}$ (kΩ·cm^2)	$R_{ct,\ ECSA}$ (kΩ·cm^2)	k^0 (cm/s)
Bare ITO	36.8	10.4	10.3	2.56×10^{-6}
ITO 20 μg	13.0	3.69	9.91	2.74×10^{-6}
ITO 50 μg	8.57	2.42	22.5	1.22×10^{-6}
ITO 100 μg	9.89	2.80	54.7	5.19×10^{-7}

Oxygen reduction reaction (ORR) was selected as another complex reaction for testing. It is a critical cathodic reaction in various fuel cells and biosensors.[93] The reaction involves four electron and four protons when fully reduced into H_2O, and two electrons and two protons when partially reduced into H_2O_2. The reaction mechanism involves adsorption of O_2 molecule onto the electrode and series of complex protonation, electron transfer and dissociation reactions.

The result of ORR on nanoporous ITO nanocube electrodes can be seen in Figure 1.14 and Table 1.4. From the cyclic voltammogram in Figure 1.14A, the general trend where seemingly electrodes with higher loadings displayed more negative reductive current and positive onset potential when the current was normalized with GSA. The cathodic current between -1.2 V and -1.0 V increased with higher loading and was seen as a strange hump. Since no such current was observed at the potential in N_2 purged electrodes, this was not hydrogen evolution reaction. Rather, such stepped current curves resembled polarization plot of partial oxygen reduction into H_2O_2, commonly seen in slow noncatalytic materials such as many undoped carbon electrodes.[94] When the current was normalized with ECSA, the trend completely reverses, where the onset potential of bare ITO glass electrode was the most positive, while becoming less positive with higher ITO nanocube loading. The ECSA normalized Nyquist plot in Figure 1.14D and calculated results from Table 4 show that highest k^0 value was observed for 20 μg loading, while 100 μg loading displayed the slowest electron transfer, very similar to the results from ascorbic acid oxidation. As in the case of ascorbic acid, ORR is one of the most studied inner electron transfer reactions, which requires adsorption of oxygen onto the electrode. The inertness of ITO as an electrode material would be highly undesirable for electrocatalysis. The thicker porous electrode layer seems ineffective in promoting faster electron transfer, rather impeding in the case of thickest electrode with 100 μg loading.

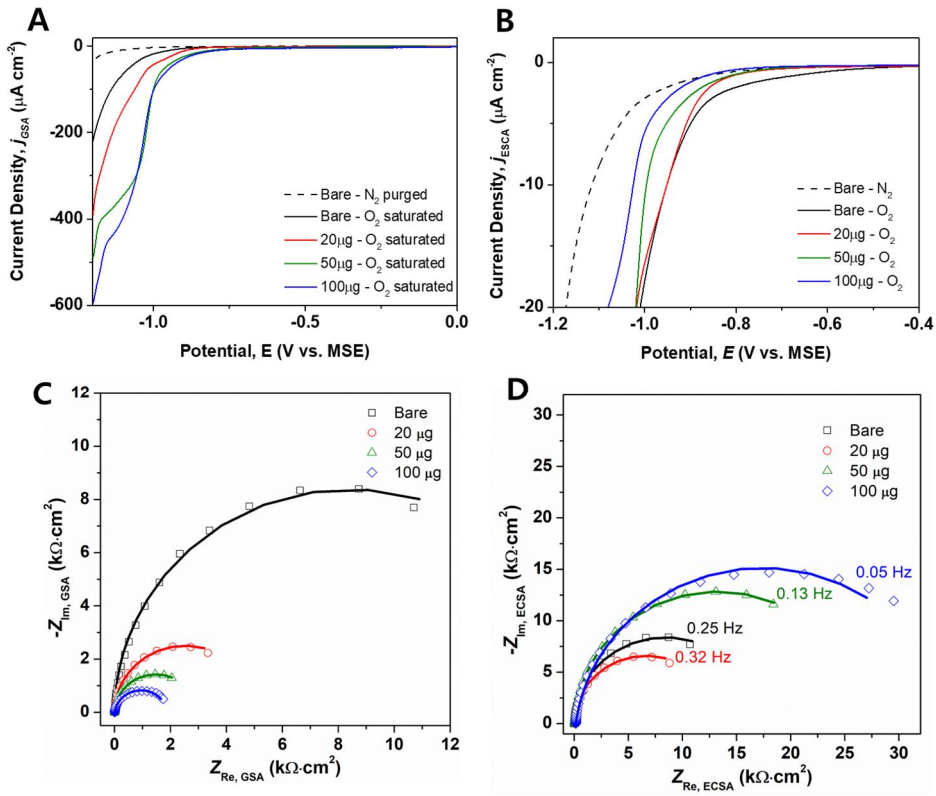

Figure 1.14 Linear sweep voltammograms of ORR on bare and nanoporous ITO electrodes where current was normalized with (A) GSA and (B) ESCA. Nyquist Plots of ORR on the same electrodes with impedance normalized with (C) GSA and (D) ESCA. The ORR experiments were carried out in 0.1 M H_2SO_4.

Table 1.4 Values obtained from fitting ORR results from Figure 1.14.

Electrode	R_{ct} (kΩ)	$R_{ct,\ GSA}$ (kΩ·cm^2)	$R_{ct,\ ECSA}$ (kΩ·cm^2)	k^0 (cm/s)
Bare ITO	59.5	16.8	16.8	1.58×10^{-6}
ITO 20 μg	17.8	5.05	13.3	2.00×10^{-6}
ITO 50 μg	10.4	2.93	26.4	1.01×10^{-6}
ITO 100 μg	6.66	1.89	34.5	7.71×10^{-7}

These preliminary studies on inner sphere, multi-electron transfer reactions suggest that catalytic effect of geometry on porous ITO electrodes were quite limited to outer sphere electron transfer reactions such as $Fe^{2+/3+}$, probably due to the limitation of the intrinsic catalytic activity of the base material. The geometric effect of nanoporous electrodes were observed in more reactive electrode materials such as in porous electrodes made of Pt and Au[31, 45], where porous electrodes displayed various electrocatalytic properties unseen in flat electrodes. In these studies, reactions such as ORR and alcohol oxidation were all promoted in porous electrodes, suggesting that geometric effects are certainly present in inner sphere reactions. The ITO was selected to minimize the effect of adsorption to observe the geometric effects. Trying to experiment with reactions that requires adsorption, in this perspective, was somewhat contradictory to the original intensions and such unfavorable results were to be expected.

1.4. Conclusion

In this part, edge-truncated, monodisperse ITO nanocubes were successfully synthesized hydrothermally. By utilizing the natural tendency of cube-shaped nanoparticles to self-assemble into cube-like clusters, self-assembled nanoporous ITO nanocube electrodes with large and small pore size were fabricated by simple drop-casting method. The electron-transfer kinetic study of outer sphere $Fe^{2+/3+}$ redox species suggests that nanoporous ITO nanocube electrode displayed higher electrode kinetics than that of the flat bare ITO electrodes by using cyclic voltammetry and electrochemical impedance spectroscopy. Even when the results were normalized with electrochemical surface area to compensate the enlarged surface area in nanoporous nanocube electrodes, the calculated standard rate constant, k^0, of the nanoporous electrodes were still higher than that of the flat counter parts. Even, it showed greater activity than the thicker nanoporous ITO electrodes. We attribute this high activity to nanoconfinement effect caused by structurally defined nano-scale pore structures created by self-assembled ITO nanocubes. This is yet another confirmation of

nanoconfinement effect of electrocatalyst materials on the electrode reactivity. On the other hand, the inner sphere electron transfer reactions, such as ascorbic acid oxidation and oxygen reduction reaction, displayed very little to no enhancement from geometry was observed. The electrochemical inertness of ITO could have prevented adsorption, which is a crucial step in these reactions. Such results imply that geometric effect of electrode on electrocatalysis is also material dependent, when considering that previous studies on porous Pt and Au electrodes.[31, 45] For the development of economical and more efficient electrocatalysts, balanced combination of material and electrode geometry would be needed in order to maximize the full potential of the catalyst.

Part 2.
Anionic Effect on Anodic Electrochemical Deposition of Nickel Iron Oxides

2.1. Introduction

2.1.1. Development of oxygen evolution reaction catalysts

With severe climate change, ongoing wars and resource nationalism threatening the supply market, the world is experiencing unprecedented economic and political instability. The desire to shift from the current reliance on fossil fuel-based technology to a more sustainable energy production and storage is ever growing. The governments from the developed parts of the globe led by the US and the European Union have recently announced goals to achieve fully functioning hydrogen and biofuel economy, aiming for greener technology.[2, 3] The fierce competition for developing more economical and efficient high performance electrocatalysts in various energy-related applications such as water electrolysis, energy storage devices, biomass and fuel cell technology has now become a global goal of the science and engineering community.

One of the most contested research themes is water electrolysis, which generates hydrogen gas, which could be harnessed for clean energy production and fertilizer synthesis. Hydrogen evolution reaction (HER) and oxygen evolution reaction (OER) are the primary reactions in water electrolysis involving two and four electron transfer reaction, respectively. Among the two, OER have sluggish electron transfer kinetics, which has always prevented water electrolysis technology from practical applications.[95]

The OER mechanism is largely dependent on pH :

In acidic aqueous conditions, $2H_2O \rightarrow O_2\uparrow + 4H^+ + 4e^-$

In neutral to alkaline aqueous conditions, $4OH^- \rightarrow O_2\uparrow + 2H_2O + 4e^-$

Many electrocatalyst materials for OER reaction were researched, and their performances are quite dependent on the pH. For acidic OER, materials such as IrO_2 and RuO_2 are

considered as the best performing, benchmark catalyst materials.[95] However, these materials suffer from stability issues at high anodic potentials where IrO_3 and RuO_4 forms and irreversibly dissolves out. For alkaline OER, nonprecious transition metal oxides based on Ni, Fe, Co and Mn were computationally analyzed to be the better performing materials.[96, 97] Due to the scarcity and high price of Ir and Ru-based catalysts, most researches focus on these more economical options, which performs best in alkaline conditions and do not suffer from the stability issues.

2.1.2. Nickel iron oxide as an OER catalyst

Nickel iron oxide is considered to be one of the most promising transition metal electrocatalysts for OER in alkaline electrolytes, with a catalytic activity that excels many other metal oxides.[97-99] The high OER performance of nickel iron oxide was first discovered by Edison and Junger in the early 1900s, where the poisoning of $Ni(OH)_2$ electrodes with Fe impurities in alkaline batteries greatly improved OER performance. Since then, various studies on the effect of Fe impurities in nickel oxide electrodes including the effort of D.A. Corrigan in 1987 have greatly improved our understanding of the fundamental reaction mechanisms in NiFe-based electrodes and further improved the catalytic performance.[100-102] Despite the considerable efforts, the actual cause of such high performance still poorly understood, where even the role of Fe or interactions between Ni and Fe is hotly contested among researchers. Therefore, substantial understanding of the inner workings in NiFe-based catalysts remains to be resolved in order to substantially improve the catalytic performance.

Various approaches were made to prepare high performance nickel iron oxide electrocatalysts with optimized chemical compositions and structures. For examples, materials such as core–shell $NiFe_{0.1}Cr_{0.1}$ metal/metal hydroxides,[103] Ce-doped NiFe-layered double hydroxide nanosheets with carbon nanotubes,[104] $NiCeO_x$–Au,[105] W,Fe-

doped CoOOH,[106] and $Ba_{0.5}Sr_{0.5}Co_{0.8}Fe_{0.2}O_3$-"δ" perovskites[107] were developed. Although such approaches had their own improvements, the complicated composition and structures clouded clear understanding of the source of such enhancement. Rather, recent simpler methods such as slight modifications of the fabrication methods and conditions showed drastic enhancement of the catalytic performance without altering the compositions. For instance, the pulsed electrodeposition at high mass loadings developed by Batchellor et al. significantly improved water oxidation kinetics when compared to typical continuous electrodeposition.[108] Zhang et al. employed stepwise electrodeposition strategy where a Ni-based film was deposited by cathodic electrolysis and Fe species were incorporated via potential cycling after the deposition.[109] In addition, Song et al. synthesized NiFe single-layer nanosheets exfoliated from bulk NiFe layered double hydroxides and greatly enhanced the OER performance through the increase in the number of active edge sites and the increased electrical conductivity.[110]

2.1.3. Synthetic methods of nickel iron oxide catalysts

Nickel iron oxide catalysts are synthesized in variety of ways such as hydrothermal synthesis,[110, 111] photochemical metal–organic deposition,[112, 113] solution-cast methods,[98] sputter deposition,[114] and cathodic electrodeposition.[108, 115, 116] Among these methods, anodic electrodeposition is one of the facile routes of depositing the electrocatalysts. In anodic deposition, the metal precursor is subjected to anodic potentials where the metal ions in a lower oxidation state are electrochemically oxidized and the resulting metal interacts with surrounding water to form hydroxide/oxide precipitation on the electrode surface.[117, 118] The resulting oxides are sensitive to deposition parameters, where slight changes can result in various morphologies and structures.[119] This is in contrast to the cathodic electrodeposition process, where oxidation of metal ions happen chemically. In a typical cathodic electrodeposition, NO_3^- is first reduced to ammonia and hydroxide ions under cathodic potential, and the generated hydroxide ions in the vicinity of

the electrode form insoluble complexes with metal ions that precipitate.[120, 121] Anodically deposited catalysts are known for the self-repair mechanism under appropriate conditions, the electrocatalyst is regenerated in situ during the OER, which is important for long-term stability of the catalyst.[122-124] In addition, this method is advantageous due to its suitability in deposition onto other metal oxide-based electrodes, owing to the general stability of metal oxide materials at the oxidative potential.[125]

Anodic deposition of nickel iron oxide (NiFeOOH) was first pioneered by Morales-Guio et al. in 2015.[125] However, the anodically prepared nickel iron oxide electrocatalyst showed a poor OER performance with a large overpotential of 370 mV at a current density of 10 mV cm^{-2} when compared to the cathodically synthesized NiFeOOH film that had an overpotential of ~260 mV at 10 mA cm^{-2}.[108, 125] When compared to the various first-row (3d) transition metal-based catalysts prepared by the anodic deposition method, they found that the performance of NiFeOOH was inferior to CoFeOOH, which is known to have lower OER activity than NiFeOOH.[97, 126] Although the computational and experimental results from other synthetic methods suggested that NiFeOOH has superior catalytic activity to CoFeOOH, later research efforts in anodic deposition have been concentrated on the CoFeOOH.[126-128]

It is noteworthy that the maximum nickel iron oxide loading Morales-Guio et al. could achieve was only 3 μg cm^{-2}[125], which was much lower than the 20 μg cm^{-2} achieved for CoFeOOH.[126] According to them, even when the deposition time was prolonged, the loading mass of NiFeOOH was saturated at 3 μg cm^{-2}. Since the catalyst loading mass can greatly influence the overall catalytic performance, the remarkably low performance of the anodically deposited NiFeOOH could be due to the limited amount of the deposited catalyst. This suggests that the catalytic performance of anodically prepared NiFeOOH could be enhanced simply by increasing the catalyst loading.

Herein, we examined the anodic deposition process of nickel iron oxide by utilizing electrochemical quartz crystal microbalance (EQCM). We observed that the anodic deposition of nickel iron oxide was greatly influenced by the reaction mixture, where factors such as the oxidation state of the metal precursor, solution pH, and particularly anions had great influences. According to our findings, we optimized the synthetic conditions and as a result, we were able to control the amount of the deposited nickel iron oxide through controlling the deposition time, leading to a thick film with leaf-like microstructure. The catalyst synthesized under the optimized condition showed excellent water oxidation performances, one of the highest among reported NiFe-based oxides on planar substrates. The variables found in this study presents a way of understanding the overall anodic deposition process and ways to enhance deposition and ultimately improve OER electrocatalytic activity.

2.2. Experimental Section

2.2.1. Anodic deposition of Ni, Fe, and nickel iron oxides

Anodic deposition was conducted using a CHI440 electrochemical workstation equipped with an oscillator and a CHI660A electrochemical workstation (CH Instruments, USA). A Pt wire and Ag/AgCl filled with 3 M NaCl were employed as the counter and reference electrodes, respectively. The Pt counter electrode was separated from the deposition solution using a glass frit to prevent the precipitation of metal ions in the solution by the generation of hydroxide ions at the Pt electrode. A nickel iron oxide film was deposited on a polycrystalline Au electrode and a Au-coated Si wafer. Microgravimetric measurements were conducted using an EQCM. An 8-MHz AT-cut quartz crystal coated with a gold film (RenLux Crystal) was used as the working electrode to measure the shift of the quartz

resonance frequency over time. The film mass (Δm) was calculated from the shift in the measured frequency (Δf) using the Sauerbrey equation,

$$\Delta \mathrm{m} = -\frac{A\sqrt{\rho_q \mu_q}}{2f_0^2} \times \Delta f$$

where A is the electrode area, ρ_q is the density of quartz (2.648 g cm^{-3}), μ_q is the shear modulus of quartz (2.947 × 10^{11} g cm^{-1} s^{-2}), and f_0 is the resonance frequency of the crystal.[129]

2.2.2. Physical characterization

The morphologies and thicknesses of the nickel iron oxide films were examined by focused ion beam-field-emission scanning electron microscopy (FIB-FE-SEM; Carl Zeiss, Germany) at the National Instrumentation Center for Environmental Management of Seoul National University. The cross-section of each catalyst film was prepared using an FIB. A top Pt layer was deposited to protect the catalyst film from the damage induced by the FIB during the milling process and employed for imaging purposes only. X-ray photoelectron spectroscopy (XPS) measurements were conducted using a SIGMA PROBE (Thermo Fisher Scientific, UK) photometer equipped with a monochromatic Al Kα X-ray source (hν = 1486.6 eV). All binding energies were corrected with respect to the position of adventitious C 1s at 284.8 eV. X-ray diffraction (XRD) patterns were recorded using a D8 Advance X-ray diffractometer (Bruker, USA) at the Research Institute of Advanced Materials.

2.2.3. Electrochemical measurements

All electrochemical measurements were conducted using CHI440 and CHI660A electrochemical workstations. A polycrystalline Au electrode was used as the working electrode. A Pt wire and Hg/HgO filled with 20% KOH were used as the counter and reference electrodes, respectively. The scale of the Hg/HgO reference electrode was

calibrated against a reversible hydrogen electrode (RHE) (0.875 V vs. RHE) using Pt wires as the working and counter electrodes in H_2-saturated 1 M KOH electrolyte. The potential was corrected for the uncompensated series resistance (R_u), which was determined by potentiostatic electrochemical impedance measurements. The overpotential (η) was calculated as $\eta = E_{measured} - E_{rev} - iR_u$, where $E_{measured}$ is the recorded potential (vs. Hg/HgO) and E_{rev} is the reversible potential (0.355 V vs. Hg/HgO) for the OER. Cyclic voltammograms (CVs) and Tafel plots were obtained in 1 M KOH electrolyte at 10 mV s^{-2} and 0.2 mV s^{-1}, respectively. Chronopotentiometry was conducted under a constant current density of 10 mA cm^{-2} over 24 h in 1 M KOH electrolyte.

2.3. Results and Discussion

2.3.1. Anodic deposition of Ni, Fe, and nickel iron oxides

In order to investigate anodic deposition of iron oxide film, we first explored influence of various basic components. Figure 2.1 shows the CV and the corresponding mass change profile of each precursor solution composed of the metal acetate salt in 0.1 M sodium acetate buffer (NaOAc, pH 5.3). In the EQCM measurements, a gold-coated quartz electrode was used as the working electrode.

Figure 2.1a (green line) shows the CV of 16 mM Ni(II) precursor. In the low potential range of 1.0–1.3 V, only the anodic current from Au oxide formation was observed, which is very similar to that in the absence of Ni(II) ions (Figure 2.1a, black line). At 1.4 V, the current began to increase, owing to water oxidation, which involves the OER as well as anodic deposition of the metal oxide film. The reverse scan showed a larger current than the previous forward scan, which continued to increase with repeated potential cycles, as depicted in Figure 2.2. From the second scan and onwards, the broad gold oxidation peak at the low

potential range disappeared indicating no further gold oxidation takes places and all the anodic currents could be attributed to the Ni oxidation. This suggests that during potential cycling, the Au electrode surface is becoming covered with the OER-active nickel oxide film.

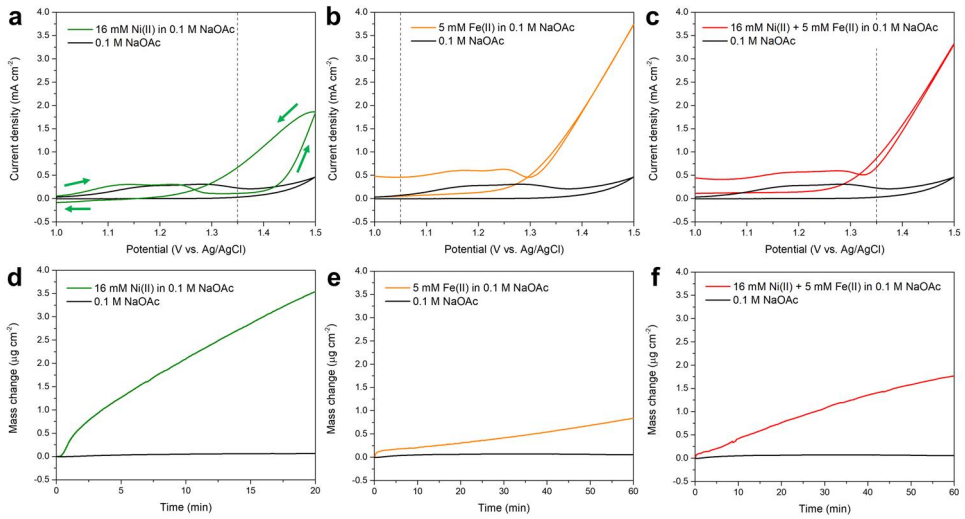

Figure 2.1. CVs and mass change profiles of 0.1 M NaOAc solution containing (a, d) 16 mM Ni(II) (green), (b, e) 5 mM Fe(II) (orange), and (c, f) 16 mM Ni(II) + 5 mM Fe(II) (red). CV and mass change profile of 0.1 M NaOAc solution are depicted in black in (a–f). pH of each solution is 5.3. Potentiostatic deposition in (b, e, f) are conducted at potentials denoted by dashed lines in (a, c, e). Arrows in (a) indicate scan direction.

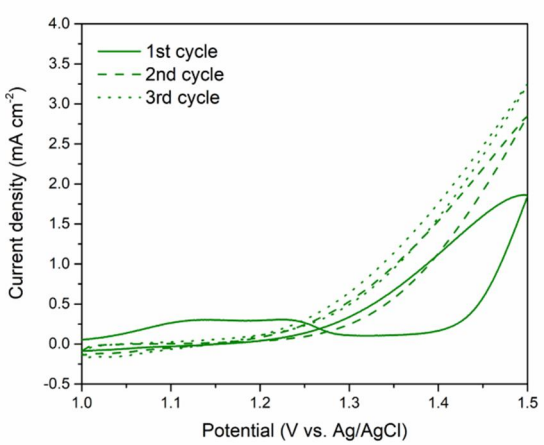

Figure 2.2. Consecutive cyclic voltammograms of 0.1 M NaOAc electrolyte with 16 mM $NiSO_4$ (pH 5.3).

Figure 2.1d shows the mass change–time curve of an Au-coated quartz electrode at a constant potential of 1.35 V immediately before the OER current starts to rise in the first forward scan. Such mass change–time curves provide information about the contribution of the water oxidation current to film formation. As shown in Figure 2.3, the corresponding current density versus time curve at 1.35 V presents a slight change in the current density at the very beginning of deposition, and the mass change behaves similarly. After a few seconds, both the current density and loading mass start to increase over time. This is followed by a current increase for a few minutes depending on the pH. Subsequently, the current reaches a plateau, whereas the mass steadily rises. Once the surface of the Au electrode is fully covered with the nickel oxide film, the newly developed surface provides a steady current density, even though its thickness continues to increase. Based on the literature, the anodic deposition of a nickel oxide film involves the electrochemical oxidation of hydroxyl ions (or water molecules) to produce adsorbed oxygen intermediates (OH_{ads}), which react with adjacent nickel ions to form the film.[130] Therefore, the deposited nickel oxide film on the Au electrode is expected to accelerate the water oxidation reaction. In addition, the formation of OH_{ads} involves a proton-coupled electron transfer step; therefore, the solution pH influences the anodic deposition of nickel oxide. As shown in Figure 2.3, the initial increase in the current density becomes steeper at higher pH.

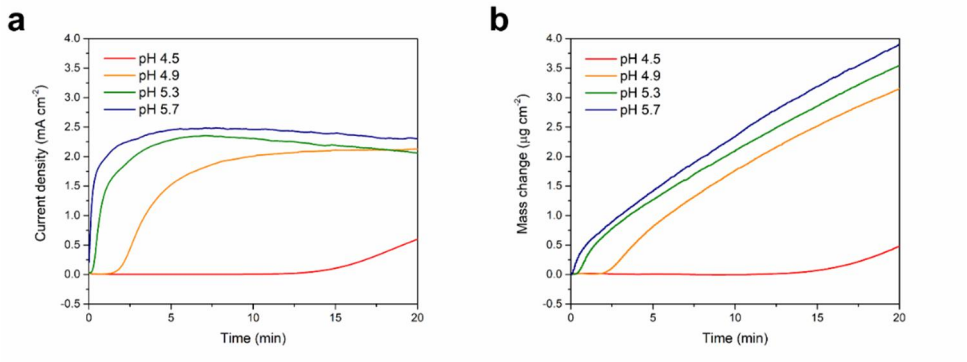

Figure 2.3. (a) Chronoamperograms and (b) mass change profiles of Au-coated quartz electrodes in 0.1 M NaOAc electrolyte with 16 mM $NiSO_4$ as a function of solution pH. Deposition in (b) was carried out at 1.35 V (vs. Ag/AgCl).

The CV of 5 mM Fe(II) is quite distinct from that of Ni(II). As shown in Figure 2.1b, a substantial anodic current appears in the low potential region of 1.0–1.1 V. To clarify the electrochemical reaction occurring in this potential region, we conducted additional CV measurements for 5 mM Fe(II) solution in a relatively lower potential range. As shown in Figure 2.4a, the redox potential of Fe(II)/Fe(III) in 0.1 M NaOAc is approximately 0.1 V, suggesting that the anodic current flowing in the low-potential region in Figure 2.1b is associated with the electrochemical oxidation of Fe(II) to Fe(III). To further examine the mechanism of the anodic deposition of FeOOH, we applied a constant potential of 1.05 V, at which the oxidation reaction of Fe(II) can occur but water oxidation cannot. As presented in Figure 2.1e, the mass of the electrode increases over 1 h, indicating that the electrochemically generated Fe(III) species is readily precipitated as γ-FeOOH on the electrode on reacting with the aqueous solvent.[131, 132] In addition, as presented in Figure 2.4b, the deposition efficiency is dependent on the solution pH. More specifically, at a pH lower than 4.9, only soluble Fe(III) species such as $Fe(OAc)_{3-y}(OH)_y$ are formed, and thus, the negligible mass change is expected.[133] At a pH higher than approximately 5, the acetate ligand is replaced

by surrounding water molecules, resulting in the precipitation of FeOOH.[131] A further increase in the solution pH accelerates the rate of FeOOH deposition.

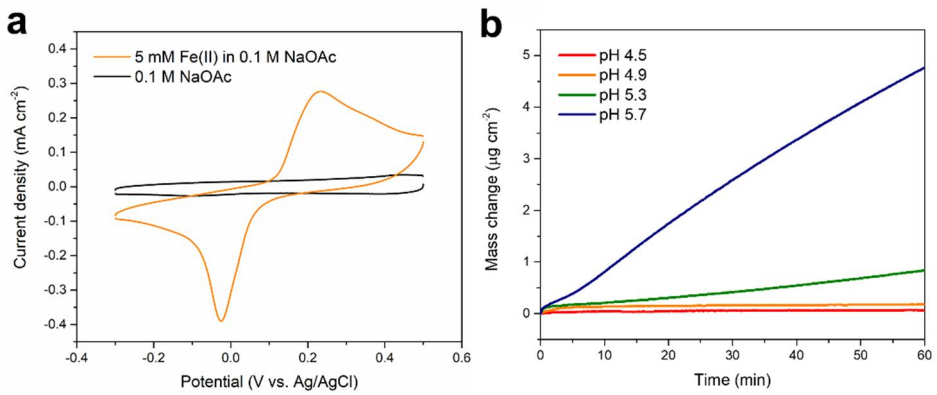

Figure 2.4. (a) Cyclic voltammograms of polycrystalline Au electrodes in 0.1 M NaOAc with 5 mM Fe(II) species (orange) and without Fe(II) species (black). All solution pH was adjusted to 5.3. (b) Mass change profiles of Au-coated quartz electrodes in 0.1 M NaOAc electrolyte with 5 mM $FeSO_4$ as a function of solution pH. Deposition was carried out at 1.05 V (vs. Ag/AgCl).

To investigate the effect of the oxidation state of the Fe precursor on the formation of FeOOH, the CV and corresponding mass change profile for Fe(III) were obtained, and the results are shown in Figure 2.5. In contrast to the CV of the Fe(II) species, no anodic current occurred in the low-potential region of 1.0–1.1 V as the Fe(III) species cannot be further oxidized in this range. Moreover, only a small increase of 0.11 μg cm^{-2} was observed in the loading mass even after 1 h of electrodeposition. This increase can be attributed to the formation of a bimetallic Au-Fe oxide/hydroxide by the incorporation of Fe(III) from the electrolyte into the AuO_x film during the electrochemical oxidation of the Au electrode surface.[134-136] The effect of the Fe(III) species is further discussed below.

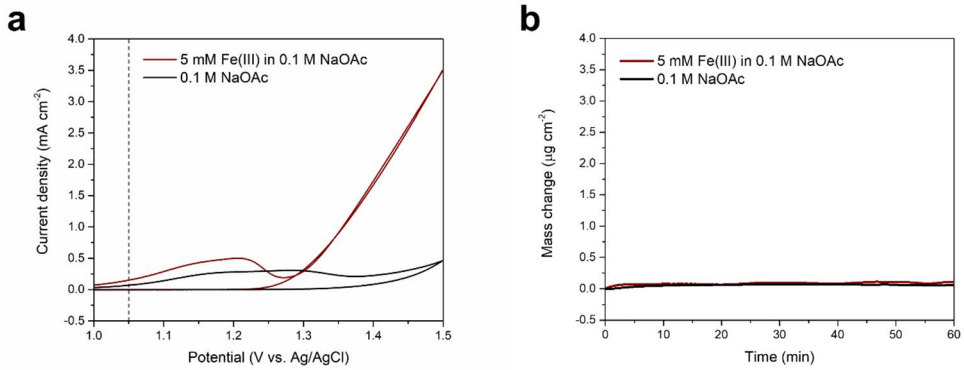

Figure 2.5. (a) Cyclic voltammograms and (b) mass change profiles of 0.1 M NaOAc solution containing 5 mM $Fe_2(SO_4)_3$ (pH 5.3). Depositions in (b) were carried out at potentials denoted as dashed lines in (a).

Figures 2.1c and f show CV and the corresponding mass change profile of a0.1 M acetate buffer solution containing 16 mM Ni(II) and 5 mM Fe(II). The CV is quite similar to that of Fe(II) except the anodic current in the low-potential region of 1.0–1.1 V, which originates from the electrochemical oxidation of Fe(II). Concurrently, the growth rate of the nickel iron oxide deposit is considerably lower than that of the deposit in the Ni(II) only. The anodic deposition of the catalyst competes with the water oxidation reaction. Because nickel iron oxide has a higher catalytic activity than NiOOH for the water oxidation reaction, the former has a lower deposition efficiency than the latter. In the nickel iron oxide composite film, the NiOOH component serves as an electrically conductive support with a high surface area, provides chemical stability, and further activates the Fe sites at which the OER occurs.[137]

To explore the effect of the Fe(III) species on the anodic deposition of nickel iron oxide, we measured the mass change profiles of a 0.1 M acetate buffer solution containing 16 mM Ni(II) and Fe(III) as a function of the Fe(III) precursor concentration. As shown in Supporting Information Figure 2.6, the deposition amount decreases as the concentration of the Fe(III) precursor increases, suggesting that the Fe(III) ions dissolved in the solution impede the

deposition. In contrast, the Fe(III) ions generated electrochemically on the electrode surface allow the deposition (Figures 2.1c and e). In this context, Morales-Guio et al. suggested that Fe(III) ions cause the corrosion of the deposit because they serve as a Lewis acid.[125] Another plausible explanation is the extremely low solubility product (K_{sp}) of Fe(III) (e.g., K_{sp} of $Fe(OH)_3 = 1.6 \times 10^{-39}$).[138] Thus, in this study, when the Fe(III) salt was added to the deposition solution, Fe(III) was readily precipitated and suspended as a colloid, instead of reacting to form a catalytic film on the electrode surface. Consequently, the deposition solution containing 16 mM Ni(II) and 5 mM Fe(III) was opaque. These results explain the formation of only ultrathin catalysts in previous studies on the anodic deposition of an Fe-containing catalyst for water oxidation, in which Fe(III) was typically used as the Fe precursor.[125-127, 139] Furthermore, these findings suggest that the use of Fe(II) instead of Fe(III) as the Fe precursor is beneficial for controlling the amount of the deposited film over a wide range, thereby allowing the formation of thicker catalyst films with a greater number of catalytically active sites. However, Morales-Guio et al. reported that an unsuccessful anodic deposition of a nickel iron oxide film when using Fe(II) sulfate as the Fe source. This suggests the presence of another factor that affects the growth of the deposit, i.e., the anion effect.[125]

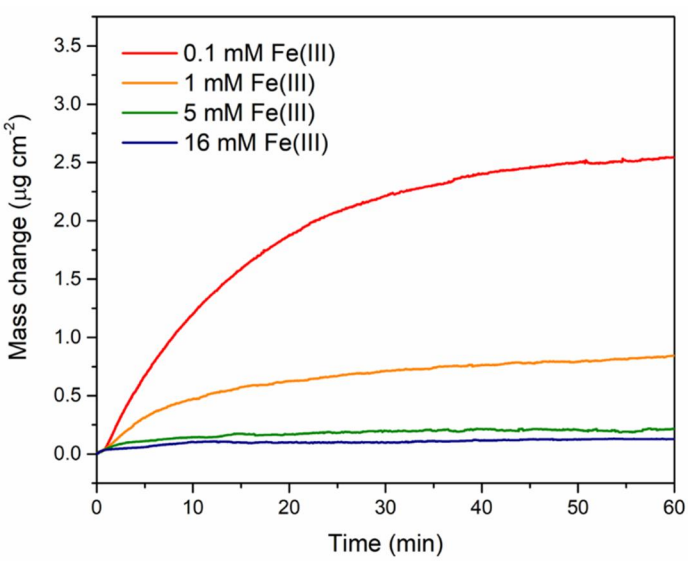

Figure 2.6. Mass change profiles of 0.1 M NaOAc solution containing 16 mM $NiSO_4$ and $Fe_2(SO_4)_3$ as a function of the concentration of $Fe_2(SO_4)_3$ at 1.35 V (vs. Ag/AgCl). All solution pH was adjusted to 5.3.

2.3.2. Effects of anions on anodic deposition of nickel iron oxide

The electrodeposition process is known to be significantly influenced by the anions present in the solution owing to their complexation with the metal.[99] To probe the effects of the anionic species on the anodic deposition process, we compared acetate and sulfate ions, which are commonly used in electroplating.

Figures 2.7a and d show that in the sulfate-only solution, both the current in voltammetry and growth rate of nickel iron oxide in the EQCM measurements are lower (entry 1 in Table 2.1; orange) than in the acetate-only solution (entry 2 in Table 2.1; red). Noticeably, sulfate ions without acetate are unfavorable for the deposition. Interestingly, the mixture of sulfate and acetate yields the highest anodic deposition and current (entry 3 in Table 1; green). Both anions work cooperatively to facilitate the Faradaic current and anodic deposition of nickel iron oxide.

To examine the role of the ionic strength of the electrolyte, control experiments were conducted in 0.2 M and 0.4 M acetate solutions (entries 4 and 5 of Table 1, respectively). Figures 2.7b and e show that the growth rate of nickel iron oxide decreases with increasing ionic strength of the acetate solution. Thus, the possibility that the higher deposition rate on the addition of sulfate to the acetate solution originates from the increased ionic strength can be excluded. It can be inferred that excessive acetate ions instead impede the growth of the deposit.

Table 2.1. Compositions of the deposition baths used to see the effects of anions on the

anodic deposition of nickel iron oxide

Entry	16 mM Ni	5 mM Fe	Electrolyte (M)
1	Ni(OAc)2	$Fe(OAc)_2$	NaOAc (0.1)
2	NiSO4	$FeSO_4$	Na_2SO_4 (0.1)
3	NiSO4	$FeSO_4$	NaOAc (0.1) + Na_2SO_4 (0.1)
4	Ni(OAc)2	Fe(OAc)2	NaOAc (0.2)
5	Ni(OAc)2	$Fe(OAc)_2$	NaOAc (0.4)
6	Ni(OAc)2	$Fe(OAc)_2$	NaOAc (0.1) + Na_2SO_4 (0.1)

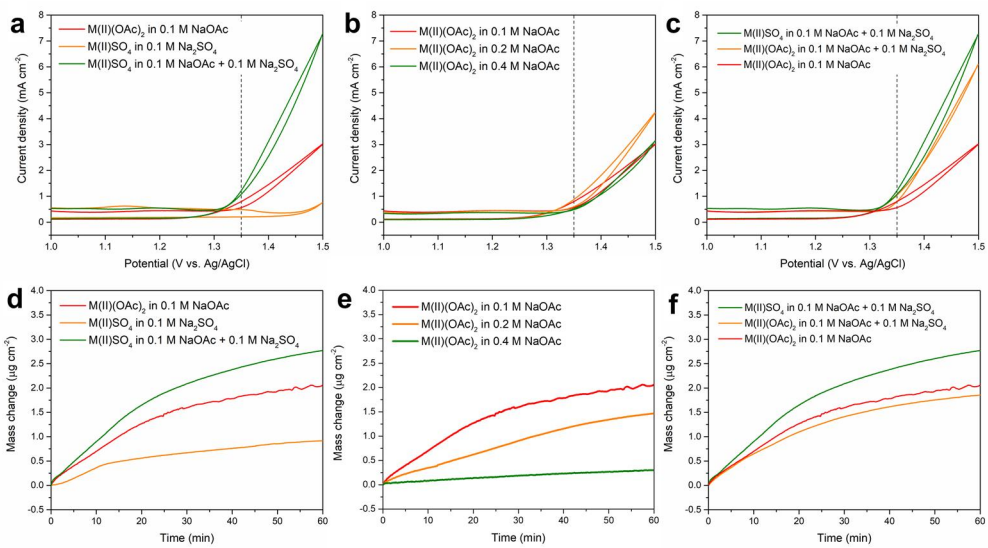

Figure 2.7. Effects of different anions on the anodic deposition of nickel iron oxide. (a) Cyclic voltammograms and (d) mass change profiles of entry 1 (red), entry 2 (orange), and entry 3 (green) of Table 1. (b) Cyclic voltammograms and (e) mass change profiles of entry 1 (red), entry 4 (orange), and entry 5 of Table 1. (c) Cyclic voltammograms and (f) mass change profiles of entry 3 (green), entry 6 (orange), and entry 1 (red) of Table 1. All solutions possessed a pH of 5.3. The potentiostatic depositions in (d, e, f) were carried out at 1.35V vs. Ag/AgCl, denoted by the dashed lines in (a, b, c). M(II) represents 16 mM Ni(II) and 5 mM Fe(II) of metal salt precursors.

The effect of the counter anion of the metal precursor on the anodic deposition process was investigated. As shown in Figure 2.7c, the oxidative current in the CVs of 0.1 M NaOAc + 0.1 M Na_2SO_4 (orange and green) is significantly higher than that in those of 0.1 M NaOAc (red), suggesting that the electrolyte composition is more influential the precursor anion. However, the mass change profiles in Figure 2.7f show that the actual electrodeposition is highly dependent on the counter anions of the metal salts. When metal acetates are used as the metal precursors, a very small difference in the growth rate is observed, regardless of the electrolyte composition (red and orange), whereas the metal sulfate precursors significantly enhance the film growth. These results suggest that the precursor anion has a strong effect on the deposition process.

The chemical speciation in each deposition solution us identified referring to the stability constants (β_n) for the formation of metal ion complexes with acetate or sulfate ions as can be seen in Table 2.2.[140]

The stability constant for the reaction $M + nL \rightleftharpoons ML_n$ is expressed as follow:

$$\beta_n = \frac{[ML_n]}{[M][L]^n}$$

where M is metal ion and L is coordination ligand

Based on the stability constants, sulfate ions are more probable to associate with Ni(II) and Fe(II) than acetate ions. It should be noted that sulfate ions are not typically considered to be coordination ligands but as counter anions in ion pairs of hydrated metal ions. The stability constants also indicate that although acetate ions are less probable to associate with the metal ions, they can immediately coordinate as ligands, even when acetate and sulfate ions coexist in the deposition solution.

Table 2.2. Stability constant (β_n) for the formation of complex[140]

Metal ion	Log β_n
Acetate	
Ni^{2+}	1.43
Fe^{2+}	1.40
Sulfate	
Ni^{2+}	2.32
Fe^{2+}	2.2

In general, electro-inactive ligands in coordination complexes, except those undergoing metal-to-ligand charge transfer, facilitate the oxidation of the central metal ion. Moreover, such ligands insert themselves between metal ions and an electrode, to prevent direct contact. Therefore, outer-sphere electron transfer is more probable than inner-sphere electron transfer during heterogeneous electron transfer events. For instance, it has been reported that when ethylenediaminetetraacetic acid, a representative ligand with a highly strong coordination capability, is added to the deposition solution, the overpotential for the oxidation of the central metal ion drastically decreases; however, there is no film formation.[141] In contrast, our anodic deposition experiments of nickel iron oxide suggest that despite their high stability constant with the central metal ion, sulfate ions allow easy excess to it, enhancing the film growth while facilitating water oxidation. This can be also understood based on ionic kosmotropes (water structure-makers) and ionic chaotropes (water structure-breakers), terms introduced by Collins and Washbough to explain the effects of different electrolytes on the viscosity of water.[142] According to their report, a sulfate ion is a representative kosmotropic ion, which exhibits strong interactions with water molecules and is tightly hydrated, thereby increasing the viscosity of the solution. Studies using dielectric relaxation spectroscopy and ultrasonic absorption techniques also found that a sulfate ion is strongly

hydrated and tends to form a noncontact ion pair with one or two solvent molecules between it and the metal cation. Some examples are a double-solvent-separated ion pair ($M^{m+}(OH_2)(OH_2)(SO_4^{2-})$) and a solvent-shared ion pair ($M^{m+}(OH_2)(OH_2)(SO_4^{2-})$).[143, 144] In contrast, an acetate ion is a chaotropic ion that tends to coordinate metal ions directly, instead of forming ion pairs.[145] For Ni^{2+} and Fe^{2+} in aqueous media, acetate is considered to behave as a coordination ligand.

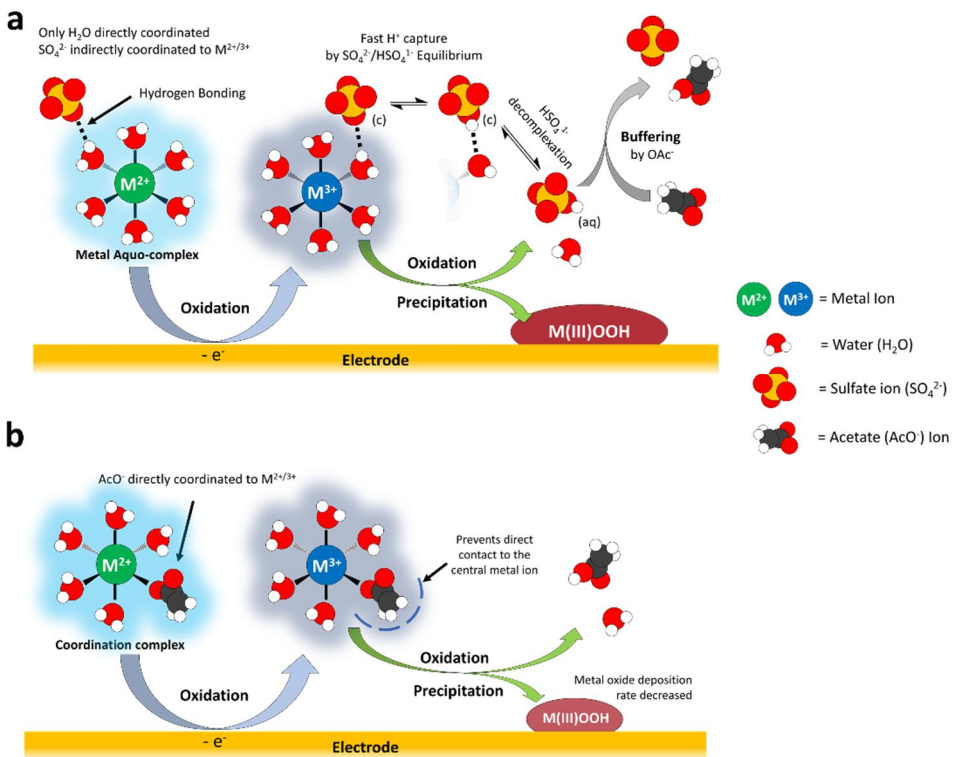

Figure 2.8. Proposed mechanism for the anodic deposition of NiFeOOH when (a) metal sulfate precursor and (b) metal acetate is used respectively.

Figure 2.8 shows the proposed mechanisms for the anodic deposition of nickel iron oxide and their dependence on the precursor anions used. Because of the kosmotropic nature of an aqueous sulfate ion, it is speculated that the central metal ion is completely surrounded by water molecules, forming a metal aquo complex. A sulfate ion is indirectly bound to the

complex via hydrogen bonding with a water molecule in the first hydration layer, as illustrated in Figure 2.8a. The central metal first oxidizes at the oxidation potential. On reaching a higher water anodization potential, the OER occurs, and the water molecules directly bound to the metal ion are oxidized. Oxidation of the transition metal ion is known to lower the p*K*a, i.e., increasing the chance of deprotonation. The literature p*K*a value of Fe^{2+} is around 9.5 whereas p*K*a of Fe^{3+} ion is generally around 2.2 to 2.5, which is not very far from the p*K*a value of HSO^{4-} ion (p*K*a = 1.92 ~ 2.00).[146-150] In the case of Ni ions, the p*K*a of Ni^{2+} aquo-complex is about 9.8, but p*K*a value for Ni^{3+} ions is largely unknown. We can only speculate that the acidity of Ni^{3+} aquo-complex is also highly acidic like the Fe^{3+} ions, as this is the general trend predicted from the electronegativity and its relationship with the p*K*a.[149, 150] Because of the similarity in the p*K*a values of bisulfate and 3+ metal ions, we can expect the sulfate ions that are hydrogen-bonded to the water molecules composing the metal aquo-complex to accept the released hydrogen ion from the highly acidic 3+ aquo-complex. Accepting the above assumption, the sulfate ions that are hydrogen bonded to the metal complex would probably assume a SO_4^-/HSO_4^- equilibrium and rapidly accept the hydrogen ions, thereby facilitating further oxidation. Subsequently, the bisulfate ion would be freed from the complex, and rapidly release the hydrogen atom into the bulk solution owing to its low p*K*a.

In contrast, acetate ions are expected to be directly coordinated to the central metal ion, forming a typical coordination complex, as shown in Figure 2.8b. The literature survey on the metal acetate in aqueous solution, suggests that the large proportion of metal ions is directly coordinated by a single acetate ion in a monodentate binding mode as shown in the figure although the proportion of coordinated acetate are somewhat controversial depending on the literature.[151-156] Depending on the literature, the amount of coordinated metal acetate species in the solution was about 30~80%. This large variation maybe partly due to the measuring methods, which varied from Raman or IR spectroscopy, X-ray spectroscopy to electrochemical open circuit potential measurements. The direct coordination of acetate

ion will hamper easy access to the central metal ion and reduces the oxidization rate. Consequently, water oxidation becomes unfavorable, and thus, the growth of the metal oxide decelerates.

However, the acetate ions can serve as buffering agents and maintain the solution pH during the oxide electrodeposition. As anodic deposition involves proton-coupled electron transfer processes, a proton acceptor is required to facilitate it. In addition, maintaining a steady pH condition in the vicinity of the electrode surface is critical because electrochemical water oxidation is pH-sensitive. Notably, the stability constants of the metal sulfate and metal acetate salts are comparable, and the ligands do not seem to be readily exchanged, which is explained in the next paragraph. Thus, the initial structure of the metal precursor and the presence of a buffering agent play vital roles in controlling the electrodeposition rate.

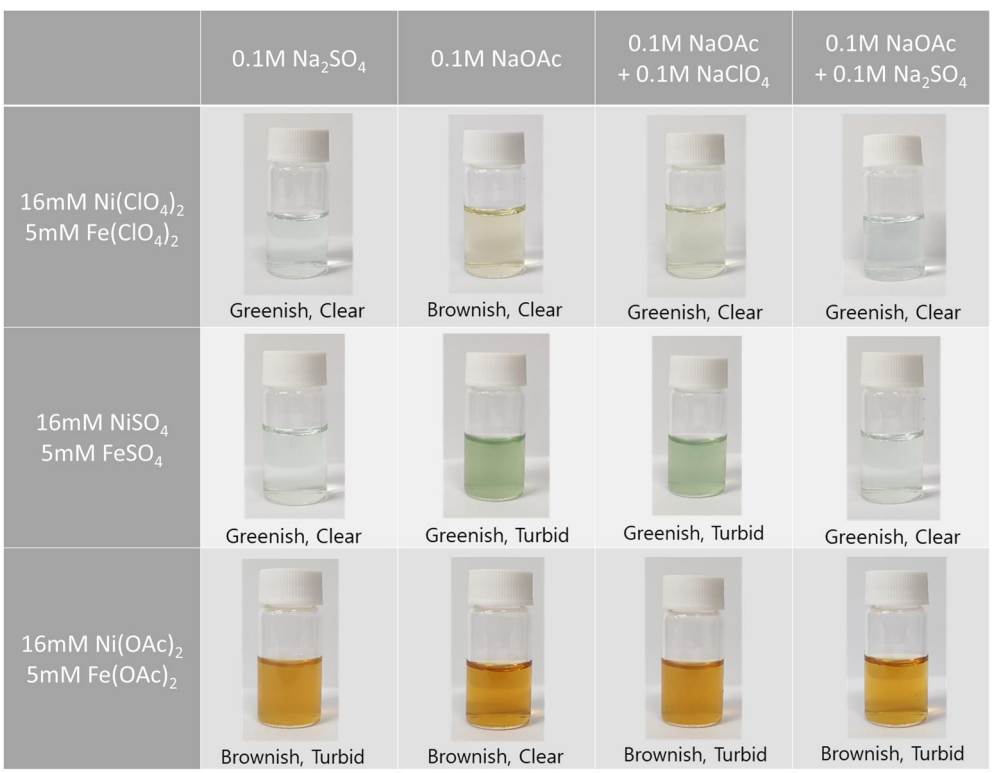

Figure 2.9. Color of the deposition solution prepared by dissolving various metal-anion salts in electrolyte with different compositions. The top row shows the electrolyte composition of

each column. The left column shows the metal salt composition of each row. pH was adjusted to about 5.3.

The colors of the deposition solutions allow observing the effects of the anion coordination strength. Perchlorate ions assist in comparative studies. They are commonly used in electrochemical measurements to avoid adsorption and complexation because of the low stability constants with various metal ions. When anions in the solution are perchlorates, we can assume that the majority of the metal ions in the solution are surrounded by the solvent, i.e., water molecules. Figure 2.9 shows the colors of the deposition solutions having various compositions. The dissolved nickel salts are greenish, typical of the Ni^{+2} oxidation state, regardless of the anionic species in the solution. In comparison, the iron salt solutions significantly vary in color depending on the anion in the solution. Iron acetate shows a strong brownish color when dissolved, whereas iron perchlorate and iron sulfate are pale green or neutral. Therefore, the color of the solution reflects whether the anionic species are bound to iron ions. The perchlorate salts appear greenish in solution, similar to the iron sulfate salt solutions. This suggests that iron ions are not coordinated by these two anions but by water molecules, which are not replaced by the 0.1 M acetate electrolyte. This agrees with the proposed model for metal–sulfate ion pairs. In contrast, iron acetate salts dissolve to become brownish, reflecting that acetate ions bind with iron ions, unlike sulfate and perchlorate ions. Although the stability constant of sulfate ions is larger than those of the other anions, the solutions containing acetate salts do not undergo any change in color, i.e., brownish, in the presence of a sulfate electrolyte. Figure 2.10 shows the UV-Visible spectrum of Fe^{2+} in aqueous solution with various anions. Iron sulfate and acetate salt have very distinct colors so any change the spectrum can be interpreted as a change in complexation. However, even when they were mixed in a solution with different anions and was gently stirred for 1 h, both solutions still retained the initial spectrum, supporting the above assumption that anions bound to the metal ion does not readily mix or interchange with the free anions in the solution.

This result also supports our observations in electrochemical tests in Figure 2.7 where the deposition yields highly depended on the anion in the metal precursor.

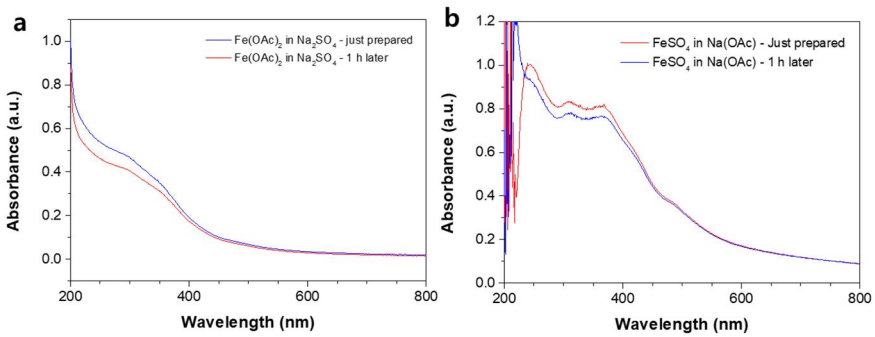

Figure 2.10. UV-Visible spectrum of aqueous solution of Fe salts in different anionic environment. Spectrum of just prepared solution and the solution after 1 hour of mixing was measured for (a) $FeSO_4$ in NaOAc and (b) $Fe(OAc)_2$ in Na_2SO_4 solutions.

Moreover, the turbidity of the solutions in Figure 2.9 also suggest other possibilities in the mechanism. Fe ions are prone to formation of hydroxide species that are well known for oligomer formation and precipitation.[157, 158] In that sense, the turbidity would mean the solution maybe undergoing formation of these large particulates. This will slightly change the proposed mechanism in Figure 2.8 where the ferric hydroxide would quickly precipitate onto the electrode surface first and act as a nucleation center for the film growth. In order to prevent the autooxidation of Fe^{2+} ions and hydrolysis from happening, deposition solutions were bubbled with N_2 gas before the experiments. If not purged of O_2 and intentionally left to chemically oxidize, precipitation mainly due to the chemical oxidation and precipitation of iron hydroxide occurs, and this can easily be observed in the EQCM results as an abnormal increase in weight when compared to the oxidation current. Although the effect from the chemical oxidation of Fe^{2+} ions cannot be ruled out, the effect seems to be small with the N_2 bubbling since the deposition seems to depend on the total oxidation charge.

As shown in Figure 2.11, the acetate salt solution presents the lowest oxidative current and mass change profiles in 0.1 M NaOAc and 0.1 M Na_2SO_4. The solutions of the sulfate and perchlorate salts produce higher currents and mass loadings than the acetate salts in the same electrolyte. The sulfate salts produce a higher current than the perchlorate salts, whereas the former reverse the trend of the masses of the deposits. Compared with perchlorate ions, sulfate ions preferentially drive water oxidation to the OER, instead of to the deposited film. The cause of this phenomenon remains unclear.

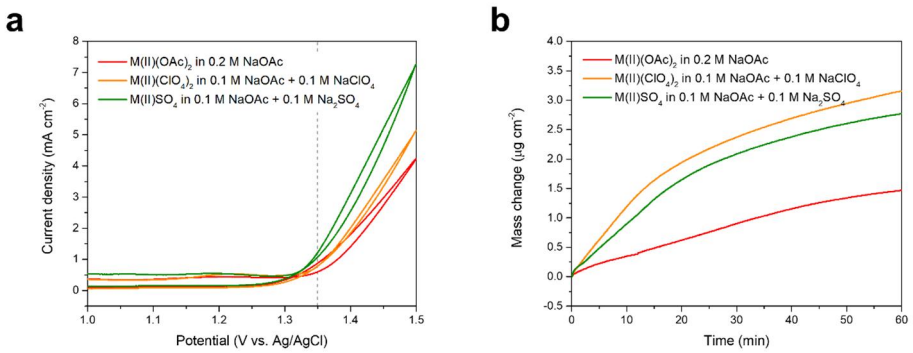

Figure 2.11. (a) Cyclic voltammograms and (b) mass change profiles of $M(II)(OAc)_2$ in 0.2 M NaOAc (red), $M(II)(ClO_4)_2$ in 0.1 M NaOAc + 0.1 M $NaClO_4$, and $M(II)SO_4$ in 0.1 M NaOAc + 0.1 M Na_2SO_4. M(II) represents 16 mM Ni(II) and 5 mM Fe(II). All solution pH was adjusted to 5.3.

It should be noted that sulfate as the sole anion in the solution yield a low current and poor electrodeposition (Figures 2.7a and c, orange). This is because the production of protons via several proton-involving reactions causes a severe decrease in the local pH near the electrode surface, as shown in Figures 2.3 and 2.4. Addition of 0.1 M NaOAc to the above-mentioned sulfate-based solution drastically increases the growth rate of the deposit and the oxidative current (Figures 2.7a and c, green). It is anticipated that any buffer agent with a higher pK_a and a lower stability constant of complexation would lead to better performance. However,

other commonly used buffers such as phosphate and bicarbonate buffers lead to the precipitation of the metal ions; thus, they could not be tested to verify this.

2.3.3. New conditions for anodic deposition of nickel iron oxide electrocatalyst

Based on the above findings, the anodic deposition conditions of nickel iron oxide were tuned to increase the catalyst loading mass, thereby maximizing the electrocatalytic performance of the OER. First, we used Fe(II) as the Fe precursor because Fe(III) hinders deposit growth, as shown in Figures 2.5 and 2.6. Metal sulfate salts were dissolved as metal precursors, and sodium acetate was added to the sulfate-based deposition solutions as a buffer reagent. Moreover, the pH was increased to approximately 7.1. Iron ions are unstable at this pH, gradually forming a colloidal phase, which appears turbid. Despite this inhomogeneity, reproducible electrodeposited nickel iron oxide films were produced. In addition, the Fe content of the deposition bath was carefully optimized. It is known that the Fe content of nickel iron oxide electrocatalysts is a critical variable for the OER performance.[99]

Figure 2.12 shows the effect of the metal concentration in the deposition solution on the film growth, demonstrating that increase in the total metal concentration can result in a thicker film. As discussed in the previous section, thicker films show enhanced water oxidation activity owing to the presence of a greater number of catalytically active sites.

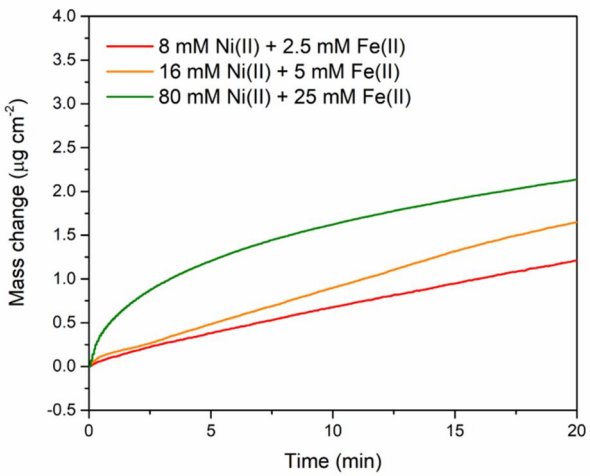

Figure 2.12. The effect of the total metal concentration in deposition solution on the growth of deposit. Deposition was carried out at 1.35 V (Ag/AgCl). All solution pH was adjusted to 5.3.

Figure 2.13 shows the OER activity of nickel iron oxide films with a loading mass of 0.2 μg cm^{-2} that are prepared in deposition baths containing various molar ratios of Ni(II) and Fe(II). It is found that the nickel iron oxide film prepared in the solution with a Ni(II):Fe(II) molar ratio of 99.5:0.5 presents the highest catalytic performance. This indicates that a very low Fe(II) content on the deposited film surface is sufficient for the electrocatalytic OER. Basically, the active sites of FeOOH need to exist on the surface, whereas those buried in the film are not expected to function significantly. Because the molar ratio of Ni(II) dominates that of Fe(II), a higher deposition rate of NiOOH at a higher pH (Figure 2.3) rapidly produces thick and porous nickel iron oxide films.

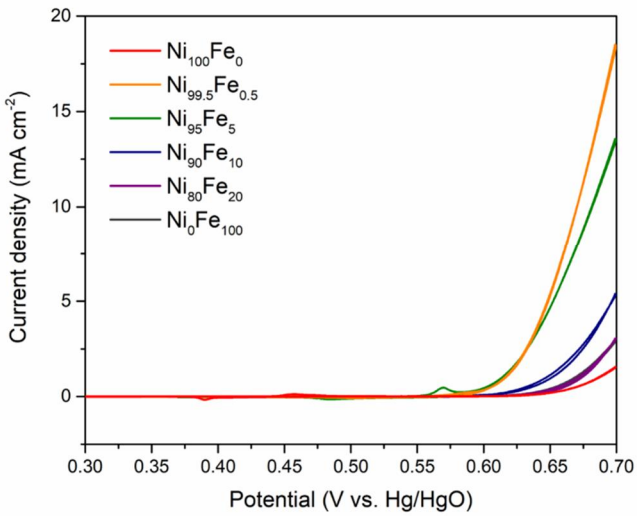

Figure 2.13. OER activities of NiFeOOH electrocatalysts with the loading mass of 0.2 μg cm^{-2} in 1 M KOH at the scan rate of 10 mV s^{-1}. The NiFeOOH electrocatalysts were deposited in the deposition baths with 0.1 M of Ni(II) and Fe(II) mixture with various molar ratios at 1.0 V (vs. Ag/AgCl).

Figure 2.14 shows the CVs obtained under previously reported deposition conditions (black) and the new ones (red). The deposition solution was redesigned to consist of 0.1 M $NiSO_4$ and $FeSO_4$ in a molar ratio of 99.5:0.5 dissolved in 0.2 M NaOAc containing 0.1 M Na_2SO_4 (pH 7.1). The concentration of NaOAc was raised to 0.2 M to increase the pH and the buffer capacity. Moreover, the deposition potential was adjusted to lower it from 1.35 V, which was applied in the previous conditions, to 1.0 V. The figure shows that the onset potentials for gold oxide formation and water oxidation are shifted to negative potentials by ca. 200 mV, which can be attributed to the difference in the solution pH. If the deposition was to be performed at the same potential (1.35 V) at such a high pH, vigorous water oxidation would impede the formation of a homogenous film by competing with metal ions for surface-adsorbed oxygen species and forming large bubbles on the electrode.

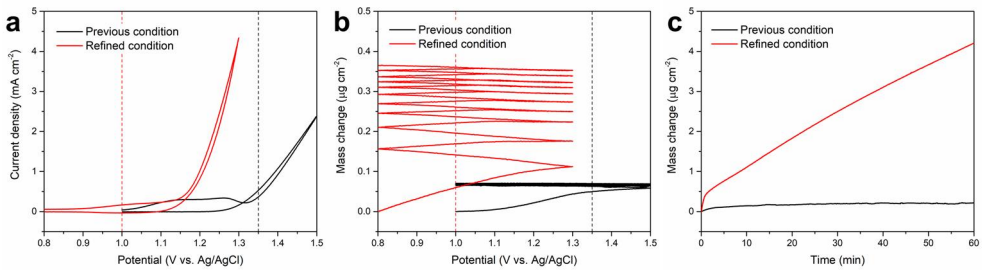

Figure 2.14. (a) Cyclic voltammograms, (b) voltmassograms, and (c) mass change profiles of the Au-coated quartz electrodes under the previously reported deposition conditions (black) and the new deposition conditions (red). while the solution previously used for anodic deposition contained 16 mM $Ni(OAc)_2$ and 5 mM $Fe_2(SO_4)_3$ dissolved in 0.1 M NaOAc (pH 5.3). The dashed lines in the cyclic voltammograms and the voltamassograms denote the potentials where the potentiostatic deposition was carried out in the mass change-time plots.

In contrast to the results presented in Figure 2.1b, only a slight current corresponding to Fe(II) oxidation flows in the low potential range of 0.8–1.0 V, which can be explained by the low concentration of the Fe(II) precursor in the deposition solution (0.5 mM $FeSO_4$). However, the voltmassograms show that the loading mass begins to increase at 0.8 V and reaches a substantial amount even with such a small amount of the Fe(II) precursor in the deposition solution (Figure 2.14b). The voltmassograms also present that the loading mass continuously increases during the five potential cycles under the new conditions, whereas it starts to increase at potentials >1.1 V under the previous conditions, becoming saturated within two cycles. The mass of the deposit formed during the five cycles under the new conditions is 0.34 μg cm^{-2}, which is much greater than that (i.e., 0.07 μg cm^{-2}) obtained under the previous conditions.

Compared with the potential cycling shown in Figure 2.14b, Figure 2.14c presents the potentiostatic deposition at 1.0 and 1.35 V conducted under the previous and new conditions, respectively. The nickel iron oxide film deposited under the new conditions grows even more rapidly, yielding a thick film of 4.2 μg cm^{-2} after 1 h, than that under the previous conditions

(c.f., 0.20 μg cm^{-2}). Moreover, the growth of the nickel iron oxide film under the new conditions continues steadily for a further 1 h without reaching saturation, thereby indicating that a thicker film can be easily produced by extending the deposition time. These results confirm that the oxidation state of the metal precursor, solution pH, anion of the metal precursor, and buffer species can drastically change the growth of nickel iron oxide films.

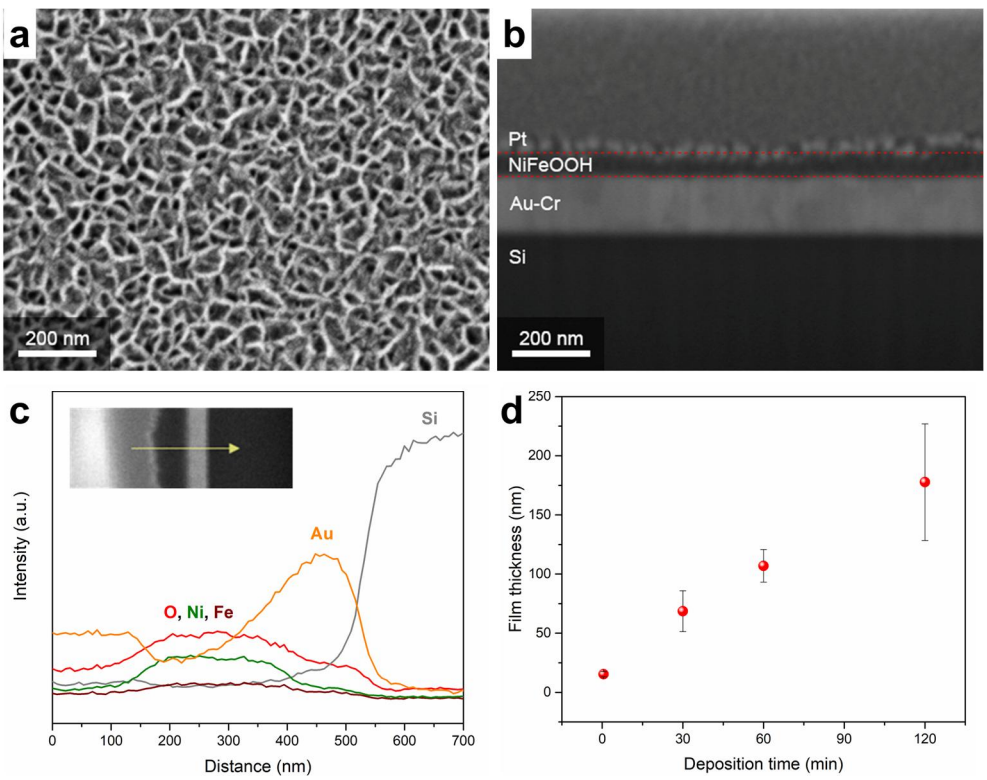

Figure 2.15. (a) Top view and (b) cross-sectional FE-SEM images of the nickel iron oxide film deposited over 30 min on Au substrate. (c) Elemental line profiles along the cross section of the nickel iron oxide film deposited over 2 h on Au substrate by energy dispersive X-ray spectroscopy. (d) Thickness of the nickel iron oxide film as a function of the deposition time. The thicknesses of the nickel iron oxide film were measured using the cross-sectional FE-SEM images.

Subsequently we examined the surface morphology of the nickel iron oxide film deposited for 30 min under the new conditions by FE-SEM. Figure 2.15a shows that nickel iron oxide

has a leaf-like morphology, which is similar to that reported in the previous literature.[137] The cross-sectional FE-SEM image shows that a uniform nickel iron oxide film is deposited on the Au substrate (Figure 2.15b). To probe the spatial distributions of different elements, elemental line profiles were obtained along the cross-section of the nickel iron oxide film deposited over 2 h on the Au substrate via energy dispersive spectroscopy. The line profile in Figure 2.15c presents that Ni, Fe, and O are uniformly distributed throughout the catalyst film. We also measured the thickness of the nickel iron oxide film deposited on the Au substrates as a function of the deposition time, using the cross-sectional FE-SEM images. Figure 2.1d demonstrates that a thick nickel iron oxide film is synthesized under the new conditions by simply varying the deposition time. This has not been achieved previously, significantly limiting the applications of anodically synthesized nickel iron oxide as an advanced catalyst until now.

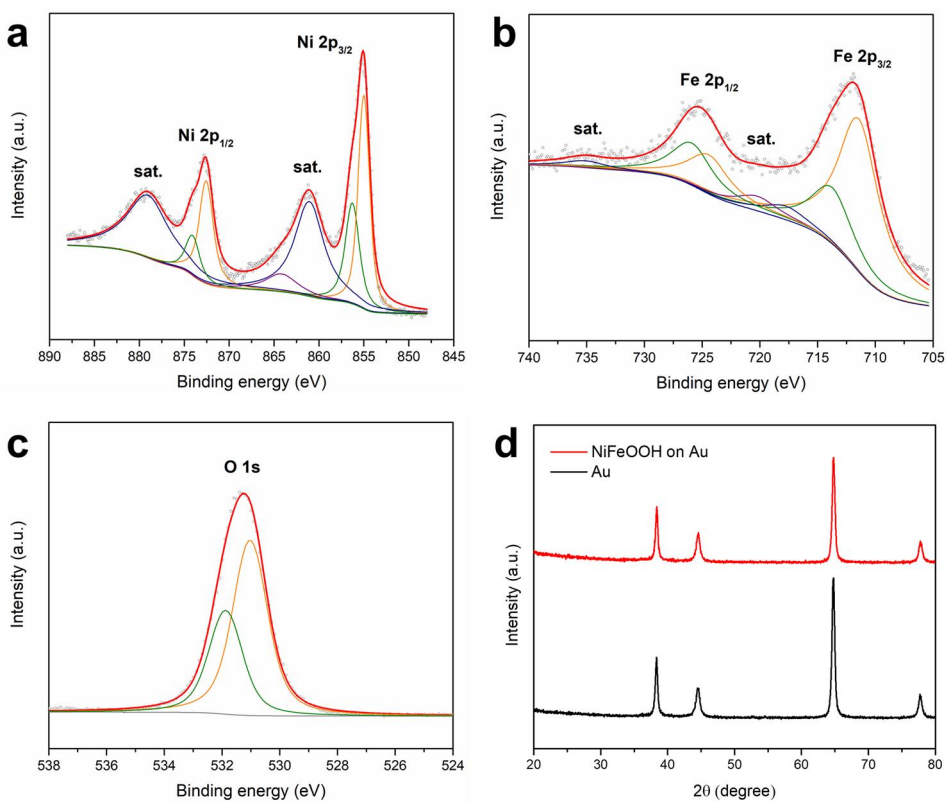

Figure 2.16. X-ray photoelectron core level spectra of (a) the Ni 2p region, (b) the Fe 2p region, and (c) the O 1s region for the nickel iron oxide film. (d) X-ray diffraction (XRD)

patterns of the nickel iron oxide film. The nickel iron oxide films were deposited over 30 min on the Au substrate.

We examined the surface chemical states and composition of the nickel iron oxide film by XPS (Figures 2.16a–c). It is found that the Ni 2p spectrum possesses two major peaks at 855.1 and 872.7 eV, which are assigned to the characteristic spin–orbit splitting of Ni(II) $2p_{3/2}$ and Ni(II) $2p_{1/2}$ with a splitting energy of 17.6 eV. The deconvoluted Ni 2p peaks at 855.0, 856.3, 872.6, and 874.1 can be assigned to Ni $2p_{3/2}$ for Ni(II) and Ni(III), indicating the presence of Ni oxide, Ni hydroxide, and Ni (oxy)hydroxide. The other two signals located at 861.1 and 879.2 eV correspond to the satellite peaks of Ni(II) $2p_{3/2}$ and Ni(II) $2p_{1/2}$, respectively (Figure 2.16a). Concurrently, the Fe 2p spectrum is composed of two main peaks located at 712.0 and 725.4 eV, which correspond to Fe $2p_{3/2}$ and Fe $2p_{1/2}$ of Fe(III), thereby revealing that iron is in the 3+ oxidation state in the film. The broad Fe $2p_{3/2}$ envelope is resolved into a surface peak at 718.2 eV and a single doublet at 711.6 and 714.2 eV for Fe(III). The other two signals centered at 720.4 and 735.4 eV correspond to the satellite peaks of Fe(III) $2p_{3/2}$ and Fe(III) $2p_{1/2}$ (Figure 2.16b). The single broad peak in the O 1s spectrum can be deconvoluted into two peaks located at 531.0 and 531.9 eV, which are assigned to OH^- and O^{2-} species present in the oxide film (Figure 2.16c).[109, 124, 125, 159] Quantitative analysis of the XPS results suggests a Ni:Fe molar ratio of 79:21, which is consistent with the reported optimal composition for the nickel iron oxide electrocatalyst exhibiting the highest OER activity.[115] There are no diffraction peaks in the XRD pattern of nickel iron oxide originating from the underlying Au substrate (Figure 2.16d). This result reflects an amorphous nature of the nickel iron oxide film.[125] Hence, the exact crystalline structure of the nickel iron oxide film synthesized using our method could not be identified.

Figure 2.17a shows the electrochemical behavior of the nickel iron oxide electrocatalysts deposited under the new conditions for different deposition times in 1 M KOH. The peak at approximately 1.42 V corresponds to the electrochemical oxidation of $Ni(OH)_2$ to

NiOOH.[115, 160] A longer deposition time leads to a substantially higher current density, which can be attributed to the higher catalyst loading. The nickel iron oxide film deposited over 2 h exhibits exceptional performance for the OER with an overpotential of 220 mV at a current density of 10 mA cm^{-2} and a Tafel slope of 29.6 mV dec^{-1} (Figure 2.17b). This performance is superior to those of state-of-the-art NiFe-based electrocatalysts mounted on planar substrates (Figure 2.17c, solid circles). Furthermore, this result is comparable to those of NiFe-based electrocatalysts supported on special architectures, such as carbon nanotubes[104] or microporous metallic Ni foam,[116] and of NiFe-based electrocatalysts containing a third element such as Co[161] or Ce[104] (Figure 2.17c, empty triangles). Details regarding the catalytic activity of the compared previously reported NiFe-based electrocatalysts are provided in Table 2.2.

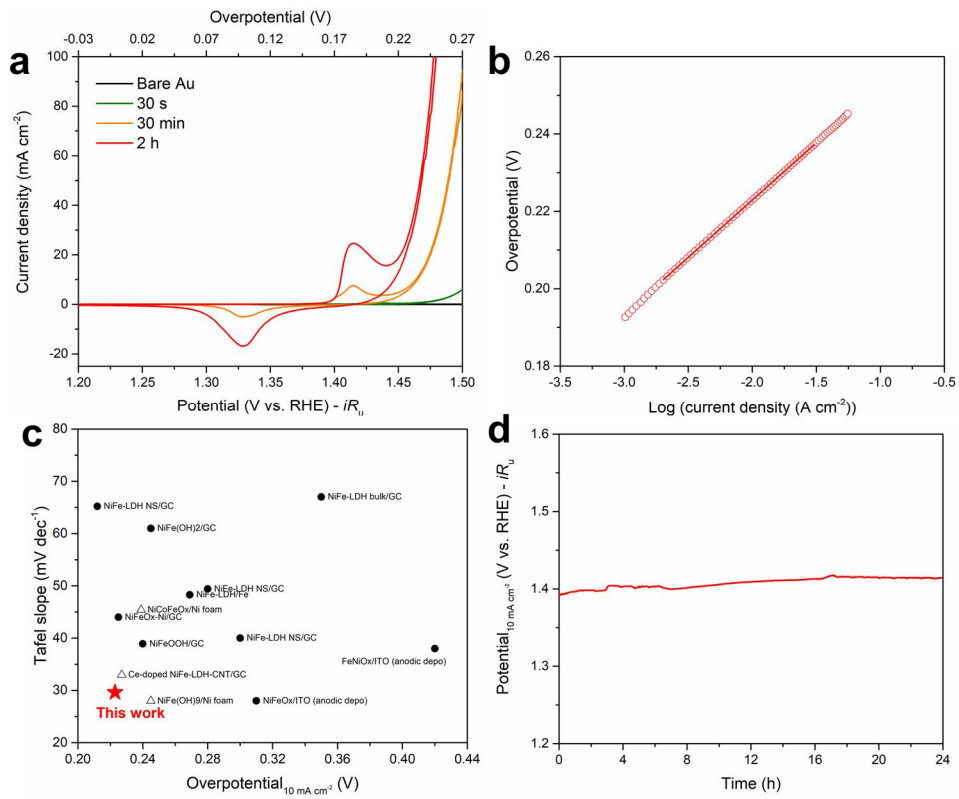

Figure 2.17. Electrochemical performance of nickel iron oxide prepared by anodic deposition under the new condition. (a) Cyclic voltammograms of nickel iron oxide as a function of the deposition time (scan rate: 10 mV s^{-1}). (b) Tafel plot of the nickel iron oxide

deposited over 2 h. (c) Comparison of catalytic the performance of the nickel iron oxide synthesized in this study with other NiFe-based electrocatalysts for the water oxidation reaction in terms of the overpotentials at 10 mA cm^{-2} and the Tafel slopes. (d) Chronopotentiometry result of nickel iron oxide at the constant current density of 10 mA cm^{-2} for 24 h.

Table 2.2. Comparison of catalytic performance of NiFe-based electrocatalysts on planar substrates

Material	Substrate	Overpotential at 10 mA cm^{-2} (mV)	Tafel slope ($mVdec^{-1}$)	Ref.
NiFeOOH	Au	223	29.6	This work
$FeNiO_x$[a]	Au	370	-	[126]
$Ni_{0.53}Fe_{0.47}O_x$[a]	ITO	310	28	[124]
$FeNiO_x$[a]	ITO	420[b]	38	[139]
NiFeOOH	Glassy carbon	240	38.9	[109]
$Ni_{0.83}Fe_{0.17}(OH)_2$	Glassy carbon	245	61	[162]
NiFe LDH bulk	Glassy carbon	350	67	[110]
NiFe LDH nanosheet	Glassy carbon	300	40	[110]
$Ni_{0.36}Fe_{2.64}O_4$/Ni	Glassy carbon	225	44	[163]
NiFe LDH	Fe plate	269	48.3	[164]
NiFe LDH nanosheet	Glassy carbon	212	65.2	[165]
NiFe LDH nanosheet	Glassy carbon	280	49.4	[166]
$Ni_3Fe(OH)_9$	Ni foam[c]	245	28	[167]
$Ni_{0.9}Co_{0.1}Fe_{0.1}O_xH_y$	Ni foam[c]	239	45.4	[168]
Ce-doped NiFe-LDH/CNT[b]	Glassy carbon	227	33	[169]

[a] NiFe-based electrocatalysts fabricated using anodic deposition method.

[b] Calculated value from Tafel plot in the literature.
[c] NiFe-based electrocatalysts supported on advanced electrode architectures or with a third element.

We believe that the outstanding performance of the nickel iron oxide film prepared in this study can be attributed to the new conditions for the anodic deposition process. The nickel iron oxide film electrodeposited on the Au substrate under the new conditions is brown, showing that the nickel in the film is probably in a 3+ oxidation state at the potential of anodic deposition occurrence (Figure 2.18).[170] This ensures that the catalyst film is electrically conductive under the anodic deposition conditions, and thus, has good electrical connectivity throughout.[137] This is expected to allow most metal sites in the catalyst film to be electrically connected and participate in the OER.

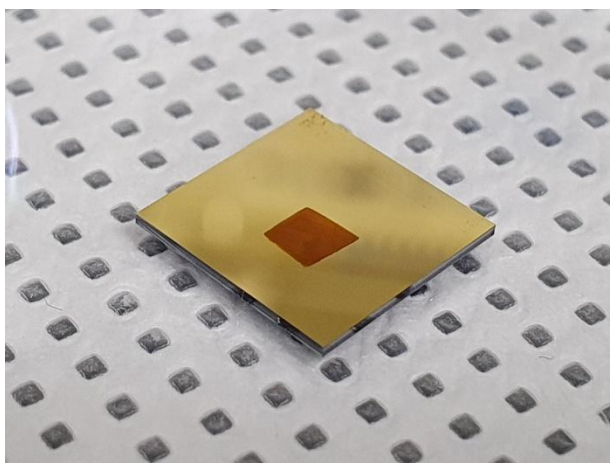

Figure. 2.18. Photograph image of as-deposited NiFeOOH on the Au substrate under the new deposition condition.

It is also notable that the overpotential of nickel iron oxide to reach a current density of 10 mA cm^{-2} decreases continuously with increasing deposition time without reaching saturation, maintaining a low Tafel slope (Figure 2.19). This suggests that the performance of nickel iron oxide can be further enhanced by increasing the deposition time. Figure 2.17d shows a negligible change in the potential at a current density of 10 mA cm^{-2} over 24 h, demonstrating excellent stability.

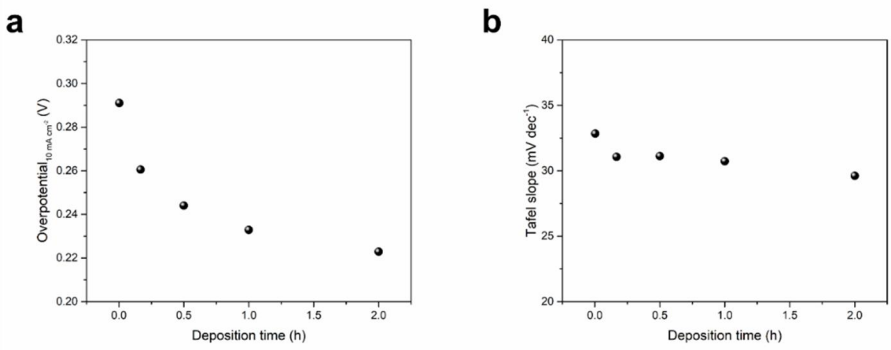

Figure 2.19. (a) Overpotential of NiFeOOH required to reach the current density of 10 mA cm^{-2} and (b) Tafel slope with the deposition time.

2.4. Conclusions

In this part, we investigated the mechanism of the anodic deposition of nickel iron oxide electrocatalyst using general electrochemical techniques combined with an EQCM. By examining the effects of anions on the anodic deposition of nickel iron oxide, we observed that the formation of the nickel iron oxide film is sensitive to the counter anion of the metal precursor. Moreover, the growth of nickel iron oxide can be substantially facilitated by the synergistic function of sulfate and acetate ions. Augmented current of water oxidation and rapid growth of a thick nickel iron oxide film can be achieved by combining a sulfate salt as a metal precursor with an acetate electrolyte serving as a buffer reagent. Based on these findings, we tuned the conditions for anodic deposition to increase the nickel iron oxide formation efficiency. This led to an almost unlimited growth of a nickel iron oxide film as a function of the deposition time. Consequently, remarkable enhancement in its electrocatalytic performance could be achieved: an overpotential of 220 mV at a current density of 10 mV cm^{-2} and a Tafel slope of 29.6 mV dec^{-1}. To our best knowledge, this is the most efficient OER catalyst performance reported until now among NiFe-based oxides on planar substrates. The electrocatalyst film possibly became thicker on prolonging the electrodeposition, and the

findings from this study suggest that the conditions for the preparation of nickel iron oxide can be modified. Further advances in anodic deposition might enable the development of non-precious metal-based electrocatalysts for realizing practical OER.

References

[1] X.X. Xu, X. Wang, Size- and Surface-Determined Transformations: From Ultrathin InOOH Nanowires to Uniform c-In2O3 Nanocubes and rh-In2O3 Nanowires, Inorg Chem, 48 (2009) 3890-3895.
[2] D.o.E. (US), DOE National Clean Hydrogen Strategy and Roadmap (Draft), (2022).
[3] E. Commision, Implementing the Repower EU Action Plan: investment needs, hydrogen accelerator and achieving the bio-methane targets, (2022).
[4] W. Li, L. Zhao, X.L. Jiang, Z.K. Chen, Y.G. Zhang, S.Y. Wang, Confinement Engineering of Electrocatalyst Surfaces and Interfaces, Adv Funct Mater, 32 (2022).
[5] L.G. Li, P.T. Wang, Q. Shao, X.Q. Huang, Recent Progress in Advanced Electrocatalyst Design for Acidic Oxygen Evolution Reaction, Adv Mater, 33 (2021).
[6] M.Q.C.O. Li, H. Huang, J.X. Low, C. Goo, R. Long, Y.J. Xiong, Recent Progress on Electrocatalyst and Photocatalyst Design for Nitrogen Reduction, Small Methods, 3 (2019).
[7] L. Yaqoob, T. Noor, N. Iqbal, Recent progress in development of efficient electrocatalyst for methanol oxidation reaction in direct methanol fuel cell, Int J Energ Res, 45 (2021) 6550-6583.
[8] Y.Y. Liu, Y.H. Wang, S.L. Zhao, Z.Y. Tang, Metal-Organic Framework-Based Nanomaterials for Electrocatalytic Oxygen Evolution, Small Methods, 6 (2022).
[9] J. Zhu, L.S. Hu, P.X. Zhao, L.Y.S. Lee, K.Y. Wong, Recent Advances in Electrocatalytic Hydrogen Evolution Using Nanoparticles, Chem Rev, 120 (2020) 851-918.
[10] C. Du, Y.J. Gao, H.Q. Chen, P. Li, S.Y. Zhu, J.G. Wang, Q.G. He, W. Chen, A Cu and Fe dual-atom nanozyme mimicking cytochrome c oxidase to boost the oxygen reduction reaction, J Mater Chem A, 8 (2020) 16994-17001.
[11] J.X. Fang, L.L. Zhang, J. Li, L. Lu, C.S. Ma, S.D. Cheng, Z.Y. Li, Q.H. Xiong, H.J. You, A general soft-enveloping strategy in the templating synthesis of mesoporous metal nanostructures, Nat Commun, 9 (2018).
[12] K. Shen, L. Zhang, X.D. Chen, L.M. Liu, D.L. Zhang, Y. Han, J.Y. Chen, J.L. Long, R. Luque, Y.W. Li, B.L. Chen, Ordered macro-microporous metal-organic framework single crystals, Science, 359 (2018) 206-+.
[13] B.Y. Guan, S.L. Zhang, X.W. Lou, Realization of Walnut-Shaped Particles with Macro-/Mesoporous Open Channels through Pore Architecture Manipulation and Their Use in Electrocatalytic Oxygen Reduction, Angew Chem Int Edit, 57 (2018) 6176-6180.
[14] R. Du, J.O. Joswig, R. Huebner, L. Zhou, W. Wei, Y. Hu, A. Eychmueller, Freeze-Thaw-Promoted Fabrication of Clean and Hierarchically Structured Noble-Metal Aerogels for Electrocatalysis and Photoelectrocatalysis, Angew Chem Int Edit, 59 (2020) 8293-8300.
[15] W. Liu, A.K. Herrmann, N.C. Bigall, P. Rodriguez, D. Wen, M. Oezaslan, T.J. Schmidt, N. Gaponik, A. Eychmuller, Noble Metal Aerogels-Synthesis, Characterization, and Application as Electrocatalysts, Accounts Chem Res, 48 (2015) 154-162.
[16] X.W. Lv, W.S. Xu, W.W. Tian, H.Y. Wang, Z.Y. Yuan, Activity Promotion of Core and Shell in Multifunctional Core-Shell Co2P@NC Electrocatalyst by Secondary Metal Doping for Water Electrolysis and Zn-Air Batteries, Small, 17 (2021).
[17] D.Y. Liu, Q. Zeng, C.Q. Hu, H. Liu, D. Chen, Y.S. Han, L. Xu, J. Yang, Core-Shell CuPd@NiPd Nanoparticles: Coupling Lateral Strain with Electronic Interaction toward High-Efficiency Electrocatalysis, Acs Catal, 12 (2022) 9092-9100.
[18] J.Y. Guan, S.X. Yang, T.T. Liu, Y.H. Yu, J. Niu, Z.P. Zhang, F. Wang, Intermetallic FePt@PtBi Core-Shell Nanoparticles for Oxygen Reduction Electrocatalysis, Angew Chem Int Edit, 60 (2021) 21899-21904.
[19] C. Chen, Y.J. Kang, Z.Y. Huo, Z.W. Zhu, W.Y. Huang, H.L.L. Xin, J.D. Snyder, D.G. Li, J.A. Herron, M. Mavrikakis, M.F. Chi, K.L. More, Y.D. Li, N.M. Markovic, G.A. Somorjai, P.D. Yang, V.R. Stamenkovic, Highly Crystalline Multimetallic Nanoframes with Three-Dimensional Electrocatalytic Surfaces, Science, 343 (2014) 1339-1343.

[20] Z. Li, R. Yu, J.L. Huang, Y.S. Shi, D.Y. Zhang, X.Y. Zhong, D.S. Wang, Y.E. Wu, Y.D. Li, Platinum-nickel frame within metal-organic framework fabricated in situ for hydrogen enrichment and molecular sieving, Nat Commun, 6 (2015).
[21] K.P. Gong, F. Du, Z.H. Xia, M. Durstock, L.M. Dai, Nitrogen-Doped Carbon Nanotube Arrays with High Electrocatalytic Activity for Oxygen Reduction, Science, 323 (2009) 760-764.
[22] W.H. He, C.H. Jiang, J.B. Wang, L.H. Lu, High-Rate Oxygen Electroreduction over Graphitic-N Species Exposed on 3D Hierarchically Porous Nitrogen-Doped Carbons, Angew Chem Int Edit, 53 (2014) 9503-9507.
[23] T. Mukhiya, A. Muthurasu, A.P. Tiwari, K. Chhetri, S.H. Chae, H. Kim, B. Dahal, B.M. Lee, H.Y. Kim, Integrating the Essence of a Metal-Organic Framework with Electrospinning: A New Approach for Making a Metal Nanoparticle Confined N-Doped Carbon Nanotubes/Porous Carbon Nanofibrous Membrane for Energy Storage and Conversion, Acs Appl Mater Inter, 13 (2021) 23732-23742.
[24] L. Wang, J.Y. Fan, Y. Liu, M.Y. Chen, Y. Lin, H.C. Bi, B.X. Liu, N.E. Shi, D.D. Xu, J.C. Bao, M. Han, Phase-Modulation of Iron/Nickel Phosphides Nanocrystals "Armored" with Porous P-Doped Carbon and Anchored on P-Doped Graphene Nanohybrids for Enhanced Overall Water Splitting, Adv Funct Mater, 31 (2021).
[25] S. Bai, Y.J. Xiong, Some recent developments in surface and interface design for photocatalytic and electrocatalytic hybrid structures, Chem Commun, 51 (2015) 10261-10271.
[26] J.W. Hong, Y. Kim, Y. Kwon, S.W. Han, Noble-Metal Nanocrystals with Controlled Facets for Electrocatalysis, Chem-Asian J, 11 (2016) 2224-2239.
[27] W. Li, D.D. Wang, Y.Q. Zhang, L. Tao, T.H. Wang, Y.Q. Zou, Y.Y. Wang, R. Chen, S.Y. Wang, Defect Engineering for Fuel-Cell Electrocatalysts, Adv Mater, 32 (2020).
[28] L. Wang, Z. Sofer, M. Pumera, Will Any Crap We Put into Graphene Increase Its Electrocatalytic Effect?, Acs Nano, 14 (2020) 21-25.
[29] M. Pumera, Materials Electrochemists' Never-Ending Quest for Efficient Electrocatalysts: The Devil Is in the Impurities, Acs Catal, 10 (2020) 7087-7092.
[30] A.R. Akbashev, Electrocatalysis Goes Nuts, Acs Catal, 12 (2022) 4296-4301.
[31] J.H. Bae, J.H. Han, T.D. Chung, Electrochemistry at nanoporous interfaces: new opportunity for electrocatalysis, Phys Chem Chem Phys, 14 (2012) 448-463.
[32] S. Park, H.C. Kim, T.D. Chung, Electrochemical analysis based on nanoporous structures, Analyst, 137 (2012) 3891-3903.
[33] M. Seo, T.D. Chung, Nanoconfinement effects in electrochemical reactions, Curr Opin Electroche, 13 (2019) 47-54.
[34] J. Wordsworth, T.M. Benedetti, S.V. Somerville, W. Schuhmann, R.D. Tilley, J.J. Gooding, The Influence of Nanoconfinement on Electrocatalysis, Angew Chem Int Edit, 61 (2022).
[35] S. Banerjee, E. Gnanamani, X. Yan, R.N. Zare, Can all bulk-phase reactions be accelerated in microdroplets?, Analyst, 142 (2017) 1399-1402.
[36] S. Mondal, S. Acharya, R. Biswas, B. Bagchi, R.N. Zare, Enhancement of reaction rate in small-sized droplets: A combined analytical and simulation study, J Chem Phys, 148 (2018).
[37] J.K. Lee, S. Kim, H.G. Nam, R.N. Zare, Microdroplet fusion mass spectrometry for fast reaction kinetics, P Natl Acad Sci USA, 112 (2015) 3898-3903.
[38] S. Banerjee, R.N. Zare, Syntheses of Isoquinoline and Substituted Quinolines in Charged Microdroplets, Angew Chem Int Edit, 54 (2015) 14795-14799.
[39] M.A. Mahmoud, R. Narayanan, M.A. El-Sayed, Enhancing Colloidal Metallic Nanocatalysis: Sharp Edges and Corners for Solid Nanoparticles and Cage Effect for Hollow Ones, Accounts Chem Res, 46 (2013) 1795-1805.
[40] M.A. Mahmoud, F. Saira, M.A. El-Sayed, Experimental Evidence For The Nanocage Effect In Catalysis With Hollow Nanoparticles, Nano Lett, 10 (2010) 3764-3769.
[41] C.W. Yen, M.A. Mahmoud, M.A. El-Sayed, Photocatalysis in Gold Nanocage

Nanoreactors, J Phys Chem A, 113 (2009) 4340-4345.
[42] K.C. Huang, R.J. White, Random Walk on a Leash: A Simple Single-Molecule Diffusion Model for Surface-Tethered Redox Molecules with Flexible Linkers, J Am Chem Soc, 135 (2013) 12808-12817.
[43] R.J. White, H.S. White, A random walk through electron-transfer kinetics., Anal Chem, 77 (2005) 214a-220a.
[44] M. Seo, J.H. Bae, D.W. Hwang, B. Kwak, J. Yun, S.Y. Lim, T.D. Chung, Catalytic Electron Transfer at Nanoporous Indium Tin Oxide Electrodes, Electrochim Acta, 258 (2017) 90-97.
[45] J.H. Bae, J.H. Han, D. Han, T.D. Chung, Effects of adsorption and confinement on nanoporous electrochemistry, Faraday Discuss, 164 (2013) 361-376.
[46] J.H. Bae, Y. Yu, M.V. Mirldn, Scanning Electrochemical Microscopy Study of Electron-Transfer Kinetics and Catalysis at Nanoporous Electrodes, J Phys Chem C, 120 (2016) 20651-20658.
[47] Z.J. Li, G. Jeanmairet, T. Mendez-Morales, M. Burbano, M. Haefele, M. Salanne, Confinement Effects on an Electron Transfer Reaction in Nanoporous Carbon Electrodes, J Phys Chem Lett, 8 (2017) 1925-1931.
[48] R.C. Remsing, I.G. McKendry, D.R. Strongin, M.L. Kein, M.J. Zdilla, Frustrated Solvation Structures Can Enhance Electron Transfer Rates, J Phys Chem Lett, 6 (2015) 4804-4808.
[49] W.H. Thompson, Solvation Dynamics and Proton Transfer in Nanoconfined Liquids, Annu Rev Phys Chem, 62 (2011) 599-619.
[50] L. Fumagalli, A. Esfandiar, R. Fabregas, S. Hu, P. Ares, A. Janardanan, Q. Yang, B. Radha, T. Taniguchi, K. Watanabe, G. Gomila, K.S. Novoselov, A.K. Geim, Anomalously low dielectric constant of confined water, Science, 360 (2018) 1339-+.
[51] C. Schaaf, S. Gekle, Spatially resolved dielectric constant of confined water and its connection to the non-local nature of bulk water, J Chem Phys, 145 (2016).
[52] S. Senapati, A. Chandra, Dielectric constant of water confined in a nanocavity, J Phys Chem B, 105 (2001) 5106-5109.
[53] J.F. Olivieri, J.T. Hynes, D. Laage, Confined Water's Dielectric Constant Reduction Is Due to the Surrounding Low Dielectric Media and Not to Interfacial Molecular Ordering, J Phys Chem Lett, 12 (2021) 4319-4326.
[54] D. Keffer, H.T. Davis, A.V. McCormick, The effect of nanopore shape on the structure and isotherms of adsorbed fluids, Adsorption, 2 (1996) 9-21.
[55] J.M.M. de la Hoz, P.B. Balbuena, Local surface structure effect on reactivity of molecules confined between metallic surfaces, Phys Chem Chem Phys, 15 (2013) 1647-1654.
[56] X. Zhong, L. Wang, Z.Z. Zhuang, X.L. Chen, J. Zheng, Y.L. Zhou, G.L. Zhuang, X.N. Li, J.G. Wang, Double Nanoporous Structure with Nanoporous PtFe Embedded in Graphene Nanopores: Highly Efficient Bifunctional Electrocatalysts for Hydrogen Evolution and Oxygen Reduction, Adv Mater Interfaces, 4 (2017).
[57] Y. Liu, K.Y. Zou, T. Zhang, X. Dai, S.X. Cao, Q. Tan, Y.Z. Chen, S.W. Guo, Y.N. Liu, Novel honeycomb-like carbons with tunable nanopores as metal-free N, O-codoped catalysts for robust oxygen reduction, Chem Eng J, 433 (2022).
[58] M.R. Akanda, A.M. Osman, M.K. Nazal, M.A. Aziz, Review-Recent Advancements in the Utilization of Indium Tin Oxide (ITO) in Electroanalysis without Surface Modification, J Electrochem Soc, 167 (2020).
[59] E.B. Aydin, M.K. Sezginturk, Indium tin oxide (ITO): A promising material in biosensing technology, Trac-Trend Anal Chem, 97 (2017) 309-315.
[60] L. El Chaar, L.A. Lamont, N. El Zein, Review of photovoltaic technologies, Renew Sust Energ Rev, 15 (2011) 2165-2175.
[61] G. Bernardo, T. Lopes, D.G. Lidzey, A. Mendes, Progress in Upscaling Organic Photovoltaic Devices, Adv Energy Mater, 11 (2021).
[62] H.W. Wang, C.F. Ting, M.K. Hung, C.H. Chiou, Y.L. Liu, Z.W. Liu, K.R. Ratinac, S.P. Ringer, Three-dimensional electrodes for dye-sensitized solar cells: synthesis of indium-tin-

oxide nanowire arrays and ITO/TiO2 core-shell nanowire arrays by electrophoretic deposition, Nanotechnology, 20 (2009).
[63] M. Davis, K. Zhang, S.R. Wang, L.J. Hope-Weeks, Enhanced electrical conductivity in mesoporous 3D indium-tin oxide materials, J Mater Chem, 22 (2012) 20163-20165.
[64] D. Fattakhova-Rohfing, T. Brezesinski, J. Rathousky, A. Feldhoff, T. Oekermann, M. Wark, B. Smarsly, Transparent conducting films of indium tin oxide with 3D mesopore architecture, Adv Mater, 18 (2006) 2980-+.
[65] J.H. Ba, D. Fattakhova-Rohlfing, A. Feldhoff, T. Brezesinski, I. Djerdj, M. Wark, M. Niederberger, Nonaqueous synthesis of uniform indium tin oxide nanocrystals and their electrical conductivity in dependence of the tin oxide concentration, Chem Mater, 18 (2006) 2848-2854.
[66] J. Lee, S. Lee, G.L. Li, M.A. Petruska, D.C. Paine, S.H. Sun, A Facile Solution-Phase Approach to Transparent and Conducting ITO Nanocrystal Assemblies, J Am Chem Soc, 134 (2012) 13410-13414.
[67] J.E. Song, D.K. Lee, H.W. Kim, Y.I. Kim, Y.S. Kang, Preparation and characterization of monodispersed indium-tin oxide nanoparticles, Colloid Surface A, 257-58 (2005) 539-542.
[68] B. Shong, N. Shin, Y.H. Lee, K.H. Ahn, Y.W. Lee, Synthesis of indium tin oxide (ITO) nanoparticles in supercritical methanol, J Supercrit Fluid, 113 (2016) 39-43.
[69] Y. Endo, T. Sasaki, K. Kanie, A. Muramatsu, Direct Preparation and Size Control of Highly Crystalline Cubic ITO Nanoparticles in a Concentrated Solution System, Chem Lett, 37 (2008) 1278-1279.
[70] K. Aneesh, C.S.R. Vusa, S. Berchmans, Dual enzyme mimicry exhibited by ITO nanocubes and their application in spectrophotometric and electrochemical sensing, Analyst, 141 (2016) 4024-4028.
[71] T.H. Kim, N.S.A. Eom, S.O. Kang, Y.H. Choa, Plasma-assisted electrolytic synthesis of In(OH)(3) nanocubes for thermal transformation into In2O3 nanocubes with a controllable Sn content, Rsc Adv, 6 (2016) 20337-20342.
[72] A. Gurlo, S. Lauterbach, G. Miehe, H.J. Kleebe, R. Riedel, Nanocubes or nanorhombohedra? Unusual crystal shapes of corundum-type indium oxide, J Phys Chem C, 112 (2008) 9209-9213.
[73] M. Epifani, P. Siciliano, A. Gurlo, N. Barsan, U. Weimar, Ambient pressure synthesis of corundum-type In2O3, J Am Chem Soc, 126 (2004) 4078-4079.
[74] J.B. Mu, C.L. Shao, Z.C. Guo, M.Y. Zhang, Z.Y. Zhang, P. Zhang, B. Chen, Y.C. Liu, In2O3 nanocubes/carbon nanofibers heterostructures with high visible light photocatalytic activity, J Mater Chem, 22 (2012) 1786-1793.
[75] S. Yamamuro, K. Sumiyama, Why do cubic nanoparticles favor a square array? Mechanism of shape-dependent arrangement in nanocube self-assemblies, Chem Phys Lett, 418 (2006) 166-169.
[76] R. Suzuki, Y. Nishi, M. Matsubara, A. Muramatsu, K. Kanie, Single-Crystalline Protrusion-Rich Indium Tin Oxide Nanoparticles with Colloidal Stability in Water for Use in Sustainable Coatings, Acs Appl Nano Mater, 3 (2020) 4870-4879.
[77] K. Kanie, T. Sasaki, M. Nakaya, A. Muramatsu, Quaternary Ammonium Hydroxide-assisted Solvothermal Synthesis of Monodispersed ITO Nanoparticles with a Cubic Shape, Chem Lett, 42 (2013) 738-740.
[78] T. Sasaki, Y. Endo, M. Nakaya, K. Kanie, A. Nagatomi, K. Tanoue, R. Nakamura, A. Muramatsu, One-step solvothermal synthesis of cubic-shaped ITO nanoparticles precisely controlled in size and shape and their electrical resistivity, J Mater Chem, 20 (2010) 8153-8157.
[79] A.K.S. Kumar, Y.F. Zhang, D.L. Li, R.G. Compton, A mini-review: How reliable is the drop casting technique?, Electrochem Commun, 121 (2020).
[80] Z.D. He, Y.X. Chen, E. Santos, W. Schmickler, The Pre-exponential Factor in Electrochemistry, Angew Chem Int Edit, 57 (2018) 7948-7956.
[81] I. Streeter, G.G. Wildgoose, L.D. Shao, R.G. Compton, Cyclic voltammetry on electrode surfaces covered with porous layers: An analysis of electron transfer kinetics at single-walled

carbon nanotube modified electrodes, Sensor Actuat B-Chem, 133 (2008) 462-466.
[82] A.J. Bard, L.R. Faulkner, H.S. White, Electrochemical methods: fundamentals and applications, John Wiley & Sons2022.
[83] G.J. Brug, A.L.G. Vandeneeden, M. Sluytersrehbach, J.H. Sluyters, The Analysis of Electrode Impedances Complicated by the Presence of a Constant Phase Element, J Electroanal Chem, 176 (1984) 275-295.
[84] A. Lasia, Electrochemical Impedance Spectroscopy and its Applications, in: B.E. Conway, J.O.M. Bockris, R.E. White (Eds.) Modern Aspects of Electrochemistry, Springer US, Boston, MA, 2002, pp. 143-248.
[85] U. Rammelt, G. Reinhard, On the Applicability of a Constant Phase Element (Cpe) to the Estimation of Roughness of Solid Metal-Electrodes, Electrochim Acta, 35 (1990) 1045-1049.
[86] S. Anantharaj, S. Noda, Appropriate Use of Electrochemical Impedance Spectroscopy in Water Splitting Electrocatalysis, Chemelectrochem, 7 (2020) 2297-2308.
[87] K. Dhara, R.M. Debiprosad, Review on nanomaterials-enabled electrochemical sensors for ascorbic acid detection, Anal Biochem, 586 (2019).
[88] J.Q. Shen, P.T. Griffiths, S.J. Campbell, B. Utinger, M. Kalberer, S.E. Paulson, Ascorbate oxidation by iron, copper and reactive oxygen species: review, model development, and derivation of key rate constants, Sci Rep-Uk, 11 (2021).
[89] S. Choi, A. Park, D. Seo, W.B. Lee, K.M. Nam, Y. Kim, J. Chang, Redox-Transition from Irreversible to Reversible Vitamin C by Pore Confinement in Microporous Carbon Network, Acs Appl Mater Inter, 14 (2022) 36557-36569.
[90] A.M. Pisoschi, A. Pop, A.I. Serban, C. Fafaneata, Electrochemical methods for ascorbic acid determination, Electrochim Acta, 121 (2014) 443-460.
[91] M. Brezina, T. Loucka, J. Koryta, Marsikov.D, J. Pradac, Adsorption and Kinetics of Oxidation of Ascorbic-Acid at Platinum-Electrodes, J Electroanal Chem, 40 (1972) 13-&.
[92] A.A. Arrocha-Arcos, M. Miranda-Hernandez, Multiwalled Carbon Nanotubes anode with low oxygen content for ascorbic acid fuel cells design, Int J Hydrogen Energ, 43 (2018) 7372-7380.
[93] A. Kulkarni, S. Siahrostami, A. Patel, J.K. Norskov, Understanding Catalytic Activity Trends in the Oxygen Reduction Reaction, Chem Rev, 118 (2018) 2302-2312.
[94] J.X. Xu, L.H. Guan, Toward understanding the active site for oxygen reduction reaction on phosphorus-encapsulated single-walled carbon nanotubes, Rsc Adv, 3 (2013) 5577-5582.
[95] N.T. Suen, S.F. Hung, Q. Quan, N. Zhang, Y.J. Xu, H.M. Chen, Electrocatalysis for the oxygen evolution reaction: recent development and future perspectives, Chem Soc Rev, 46 (2017) 337-365.
[96] X.H. Xie, L. Du, L.T. Yon, S.Y. Park, Y. Qiu, J. Sokolowski, W. Wang, Y.Y. Shao, Oxygen Evolution Reaction in Alkaline Environment: Material Challenges and Solutions, Adv Funct Mater, 32 (2022).
[97] M.S. Burke, S.H. Zou, L.J. Enman, J.E. Kellon, C.A. Gabor, E. Pledger, S.W. Boettcher, Revised Oxygen Evolution Reaction Activity Trends for First-Row Transition-Metal (Oxy)hydroxides in Alkaline Media, J Phys Chem Lett, 6 (2015) 3737-3742.
[98] L. Trotochaud, J.K. Ranney, K.N. Williams, S.W. Boettcher, Solution-Cast Metal Oxide Thin Film Electrocatalysts for Oxygen Evolution, J Am Chem Soc, 134 (2012) 17253-17261.
[99] F. Dionigi, P. Strasser, NiFe-Based (Oxy)hydroxide Catalysts for Oxygen Evolution Reaction in Non-Acidic Electrolytes, Adv Energy Mater, 6 (2016) 1600621.
[100] C. Chakkaravarthy, P. Periasamy, S. Jegannathan, K.I. Vasu, The Nickel Iron Battery, J Power Sources, 35 (1991) 21-35.
[101] D.A. Corrigan, The Catalysis of the Oxygen Evolution Reaction by Iron Impurities in Thin-Film Nickel-Oxide Electrodes, J Electrochem Soc, 134 (1987) 377-384.
[102] M. Gong, H.J. Dai, A mini review of NiFe-based materials as highly active oxygen evolution reaction electrocatalysts, Nano Res, 8 (2015) 23-39.
[103] L.Z. Fan, P.L. Zhang, B.B. Zhang, Q.T. Daniel, B.J.J. Timmer, F.G. Zhang, L.C. Sun, 3D Core-Shell NiFeCr Catalyst on a Cu Nanoarray for Water Oxidation: Synergy between

Structural and Electronic Modulation, Acs Energy Lett, 3 (2018) 2865-2874.
[104] H.J. Xu, B.K. Wang, C.F. Shan, P.X. Xi, W.S. Liu, Y. Tang, Ce-Doped NiFe-Layered Double Hydroxide Ultrathin Nanosheets/Nanocarbon Hierarchical Nanocomposite as an Efficient Oxygen Evolution Catalyst, Acs Appl Mater Inter, 10 (2018) 6336-6345.
[105] J.W.D. Ng, M. Garcia-Melchor, M. Bajdich, P. Chakthranont, C. Kirk, A. Vojvodic, T.F. Jaramillo, Gold-supported cerium-doped NiOx catalysts for water oxidation, Nat Energy, 1 (2016) 16053.
[106] B. Zhang, X.L. Zheng, O. Voznyy, R. Comin, M. Bajdich, M. Garcia-Melchor, L.L. Han, J.X. Xu, M. Liu, L.R. Zheng, F.P.G. de Arquer, C.T. Dinh, F.J. Fan, M.J. Yuan, E. Yassitepe, N. Chen, T. Regier, P.F. Liu, Y.H. Li, P. De Luna, A. Janmohamed, H.L.L. Xin, H.G. Yang, A. Vojvodic, E.H. Sargent, Homogeneously dispersed multimetal oxygen-evolving catalysts, Science, 352 (2016) 333-337.
[107] J. Suntivich, K.J. May, H.A. Gasteiger, J.B. Goodenough, Y. Shao-Horn, A Perovskite Oxide Optimized for Oxygen Evolution Catalysis from Molecular Orbital Principles, Science, 334 (2011) 1383-1385.
[108] A.S. Batchellor, S.W. Boettcher, Pulse-Electrodeposited Ni-Fe (Oxy)hydroxide Oxygen Evolution Electrocatalysts with High Geometric and Intrinsic Activities at Large Mass Loadings, Acs Catal, 5 (2015) 6680-6689.
[109] W. Zhang, Y.Z. Wu, J. Qi, M.X. Chen, R. Cao, A Thin NiFe Hydroxide Film Formed by Stepwise Electrodeposition Strategy with Significantly Improved Catalytic Water Oxidation Efficiency, Adv Energy Mater, 7 (2017) 1602547.
[110] F. Song, X.L. Hu, Exfoliation of layered double hydroxides for enhanced oxygen evolution catalysis, Nat Commun, 5 (2014) 4477.
[111] Z.Y. Lu, W.W. Xu, W. Zhu, Q. Yang, X.D. Lei, J.F. Liu, Y.P. Li, X.M. Sun, X. Duan, Three-dimensional NiFe layered double hydroxide film for high-efficiency oxygen evolution reaction, Chem Commun, 50 (2014) 6479-6482.
[112] J.W. Jang, C. Du, Y.F. Ye, Y.J. Lin, X.H. Yao, J. Thorne, E. Liu, G. McMahon, J.F. Zhu, A. Javey, J.H. Guo, D.W. Wang, Enabling unassisted solar water splitting by iron oxide and silicon, Nat Commun, 6 (2015) 7447.
[113] R.D.L. Smith, M.S. Prevot, R.D. Fagan, Z.P. Zhang, P.A. Sedach, M.K.J. Siu, S. Trudel, C.P. Berlinguette, Photochemical Route for Accessing Amorphous Metal Oxide Materials for Water Oxidation Catalysis, Science, 340 (2013) 60-63.
[114] S. Klaus, M.W. Louie, L. Trotochaud, A.T. Bell, Role of Catalyst Preparation on the Electrocatalytic Activity of Ni1-xFexOOH for the Oxygen Evolution Reaction, J Phys Chem C, 119 (2015) 18303-18316.
[115] M.W. Louie, A.T. Bell, An Investigation of Thin-Film Ni-Fe Oxide Catalysts for the Electrochemical Evolution of Oxygen, J Am Chem Soc, 135 (2013) 12329-12337.
[116] X.Y. Lu, C.A. Zhao, Electrodeposition of hierarchically structured three-dimensional nickel-iron electrodes for efficient oxygen evolution at high current densities, Nat Commun, 6 (2015) 6616.
[117] Y. Surendranath, D.A. Lutterman, Y. Liu, D.G. Nocera, Nucleation, Growth, and Repair of a Cobalt-Based Oxygen Evolving Catalyst, J Am Chem Soc, 134 (2012) 6326-6336.
[118] D. Tench, L.F. Warren, Electrodeposition of Conducting Transition-Metal Oxide Hydroxide Films from Aqueous-Solution, J Electrochem Soc, 130 (1983) 869-872.
[119] M.S. Wu, C.H. Yang, M.J. Wang, Morphological and structural studies of nanoporous nickel oxide films fabricated by anodic electrochemical deposition techniques, Electrochim Acta, 54 (2008) 155-161.
[120] D.A. Corrigan, R.M. Bendert, Effect of Coprecipitated Metal-Ions on the Electrochemistry of Nickel-Hydroxide Thin-Films - Cyclic Voltammetry in 1m Koh, J Electrochem Soc, 136 (1989) 723-728.
[121] R.S. Jayashree, P.V. Kamath, Nickel hydroxide electrodeposition from nickel nitrate solutions: mechanistic studies, J Power Sources, 93 (2001) 273-278.
[122] Y.B. Kuang, Q.X. Jia, G.J. Ma, T. Hisatomi, T. Minegishi, H. Nishiyama, M. Nakabayashi, N. Shibata, T. Yamada, A. Kudo, K. Domen, Ultrastable low-bias water

splitting photoanodes via photocorrosion inhibition and in situ catalyst regeneration, Nat Energy, 2 (2017) 16191.
[123] D.A. Lutterman, Y. Surendranath, D.G. Nocera, A Self-Healing Oxygen-Evolving Catalyst, J Am Chem Soc, 131 (2009) 3838-3839.
[124] J.Y. Wang, L.L. Ji, Z.F. Chen, In Situ Rapid Formation of a Nickel-Iron-Based Electrocatalyst for Water Oxidation, Acs Catal, 6 (2016) 6987-6992.
[125] C.G. Morales-Guio, M.T. Mayer, A. Yella, S.D. Tilley, M. Gratzel, X.L. Hu, An Optically Transparent Iron Nickel Oxide Catalyst for Solar Water Splitting, J Am Chem Soc, 137 (2015) 9927-9936.
[126] C.G. Morales-Guio, L. Liardet, X.L. Hu, Oxidatively Electrodeposited Thin-Film Transition Metal (Oxy)hydroxides as Oxygen Evolution Catalysts, J Am Chem Soc, 138 (2016) 8946-8957.
[127] L. Liardet, J.E. Katz, J.S. Luo, M. Gratzel, X.L. Hu, An ultrathin cobalt-iron oxide catalyst for water oxidation on nanostructured hematite photoanodes, J Mater Chem A, 7 (2019) 6012-6020.
[128] J.F. Zhang, R. Garcia-Rodriguez, P. Cameron, S. Eslava, Role of cobalt-iron (oxy)hydroxide (CoFeOx) as oxygen evolution catalyst on hematite photoanodes, Energ Environ Sci, 11 (2018) 2972-2984.
[129] A.J. Bard, L.R. Faulkner, Electrochemical methods : fundamentals and applications, 2a ed., John Wiley & Sons, New York, 2001.
[130] G.W.D. Briggs, Fleischm.M, Anodic Deposition of Niooh from Nickel Acetate Solutions at Constant Potential, T Faraday Soc, 62 (1966) 3217-3228.
[131] K. Hashimoto, M. Cohen, Anodic Deposition of Ferric Oxyhydroxide Films on Platinum from Perchlorate Solutions, J Electrochem Soc, 121 (1974) 37-42.
[132] J.L. Leibenguth, M. Cohen, Anodic Deposition of Oxide-Films on Platinum from Ferrous Sulfate Solutions, J Electrochem Soc, 119 (1972) 987-991.
[133] C.C. Young, H.A. Laitinen, Anodic Deposition and Cathodic Stripping of Iron in Acetate Medium, Anal Chem, 44 (1972) 457-463.
[134] S. Klaus, L. Trotochaud, M.J. Cheng, M. Head-Gordon, A.T. Bell, Experimental and Computational Evidence of Highly Active Fe Impurity Sites on the Surface of Oxidized Au for the Electrocatalytic Oxidation of Water in Basic Media, Chemelectrochem, 3 (2016) 66-73.
[135] L. Trotochaud, S.L. Young, J.K. Ranney, S.W. Boettcher, Nickel-Iron Oxyhydroxide Oxygen-Evolution Electrocatalysts: The Role of Intentional and Incidental Iron Incorporation, J Am Chem Soc, 136 (2014) 6744-6753.
[136] S.H. Zou, M.S. Burke, M.G. Kast, J. Fan, N. Danilovic, S.W. Boettcher, Fe (Oxy)hydroxide Oxygen Evolution Reaction Electrocatalysis: Intrinsic Activity and the Roles of Electrical Conductivity, Substrate, and Dissolution, Chem Mater, 27 (2015) 8011-8020.
[137] M.S. Burke, L.J. Enman, A.S. Batchellor, S.H. Zou, S.W. Boettcher, Oxygen Evolution Reaction Electrocatalysis on Transition Metal Oxides and (Oxy)hydroxides: Activity Trends and Design Principles, Chem Mater, 27 (2015) 7549-7558.
[138] D.C. Harris, Quantitative chemical analysis, Seventh edition. ed., W.H. Freeman and Co, New York, N.Y, 2007.
[139] Z.H. Liang, X.B. Ge, J. Liu, An amorphous FeNiOx thin film obtained by anodic electrodeposition as an electrocatalyst toward the oxygen evolution reaction, New J Chem, 43 (2019) 19422-19428.
[140] R.M. Smith, A.E. Martell, Critical stability constants, Plenum Press, New York ; London, 1976.
[141] R.H. Jhang, C.Y. Yang, M.C. Shih, J.Q. Ho, Y.T. Tsai, C.H. Chen, Redox-assisted multicomponent deposition of ultrathin amorphous metal oxides on arbitrary substrates: highly durable cobalt manganese oxyhydroxide for efficient oxygen evolution, J Mater Chem A, 6 (2018) 17915-17928.
[142] K.D. Collins, M.W. Washabaugh, The Hofmeister Effect and the Behavior of Water at

Interfaces, Q Rev Biophys, 18 (1985) 323-422.
[143] T. Chen, G. Hefter, R. Buchner, Ion association and hydration in aqueous solutions of nickel(II) and cobalt(II) sulfate, J Solution Chem, 34 (2005) 1045-1066.
[144] G. Hefter, When spectroscopy fails: The measurement of ion pairing, Pure Appl Chem, 78 (2006) 1571-1586.
[145] B.W. Ninham, P. Lo Nostro, Knovel, Molecular forces and self assembly : in colloid, nano sciences and biology, Cambridge University Press, Cambridge, 2010.
[146] C.M. Chang, M.K. Wang, Linear relationship for acidity and stability in hexaaqua metal ions - density functional studies, Chem Phys Lett, 286 (1998) 46-50.
[147] G. Galstyan, E.W. Knapp, Computing pK(A) Values of Hexa-Aqua Transition Metal Complexes, J Comput Chem, 36 (2015) 69-78.
[148] P. George, J.P. Glusker, M. Trachtman, C.W. Bock, Linear relationships between acidity and stability in mono- and hexahydrated metal ions: a computational study, Chem Phys Lett, 351 (2002) 454-458.
[149] K. Tanaka, A. Ozaki, Acidity and Catalytic Activity of Metal Ions, B Chem Soc Jpn, 40 (1967) 1728-+.
[150] K.I. Tanaka, A. Ozaki, Acid-Base Properties and Catalytic Activity of Solid Surfaces, J Catal, 8 (1967) 1-&.
[151] R.I. Bickley, H.G.M. Edwards, S.J. Rose, R. Gustar, A Raman-Spectroscopic Study of Nickel(Ii) Acetate, Ni(Ch3coo)2 and Its Aqueous and Methanolic Solutions, J Mol Struct, 238 (1990) 15-26.
[152] Z. Nickolov, I. Ivanov, G. Georgiev, D. Stoilova, Raman study of complexation in aqueous solutions of magnesium acetate, J Mol Struct, 377 (1996) 13-17.
[153] D.A. Palmer, S.E. Drummond, Potentiometric Determination of the Molal Formation-Constants of Ferrous Acetate Complexes in Aqueous-Solutions to High-Temperatures, J Phys Chem-Us, 92 (1988) 6795-6800.
[154] D.A. Palmer, K.E. Hyde, An Experimental-Determination of Ferrous Chloride and Acetate Complexation in Aqueous-Solutions to 300-Degrees-C, Geochim Cosmochim Ac, 57 (1993) 1393-1408.
[155] K. Sawada, M. Tanaka, Aquation of Some Transition-Metal Acetates in Acetic-Acid, J Inorg Nucl Chem, 35 (1973) 2455-2464.
[156] T.J. Strathmann, S.C.B. Myneni, Speciation of aqueous Ni(II)-carboxylate and Ni(II)-fulvic acid solutions: Combined ATR-FTIR and XAFS analysis, Geochim Cosmochim Ac, 68 (2004) 3441-3458.
[157] K.H. Gayer, L. Woontner, The Solubility of Ferrous Hydroxide and Ferric Hydroxide in Acidic and Basic Media at 25-Degrees, J Phys Chem-Us, 60 (1956) 1569-1571.
[158] J. Rose, A. Manceau, A. Masion, J.Y. Bottero, Structure and mechanisms of formation of FeOOH(NO3) oligomers in the early stages of hydrolysis, Langmuir, 13 (1997) 3240-3246.
[159] L.J. Zhou, X.X. Huang, H. Chen, P.P. Jin, G.D. Li, X.X. Zou, A high surface area flower-like Ni-Fe layered double hydroxide for electrocatalytic water oxidation reaction, Dalton T, 44 (2015) 11592-11600.
[160] M.E.G. Lyons, A. Cakara, P. O'Brien, I. Godwin, R.L. Doyle, Redox, pH sensing and Electrolytic Water Splitting Properties of Electrochemically Generated Nickel Hydroxide Thin Films in Aqueous Alkaline Solution, Int J Electrochem Sc, 7 (2012) 11768-11795.
[161] Q.H. Zhao, J.L. Yang, M.Q. Liu, R. Wang, G.X. Zhang, H. Wang, H.T. Tang, C.K. Liu, Z.W. Mei, H.B. Chen, F. Pan, Tuning Electronic Push/Pull of Ni-Based Hydroxides To Enhance Hydrogen and Oxygen Evolution Reactions for Water Splitting, Acs Catal, 8 (2018) 5621-5629.
[162] Q. Zhou, Y. Chen, G. Zhao, Y. Lin, Z. Yu, X. Xu, X. Wang, H.K. Liu, W. Sun, S.X. Dou, Active-Site-Enriched Iron-Doped Nickel/Cobalt Hydroxide Nanosheets for Enhanced Oxygen Evolution Reaction, Acs Catal, 8 (2018) 5382-5390.
[163] J. Huang, J. Han, R. Wang, Y. Zhang, X. Wang, X. Zhang, Z. Zhang, Y. Zhang, B. Song, S. Jin, Improving Electrocatalysts for Oxygen Evolution Using NixFe3–xO4/Ni Hybrid Nanostructures Formed by Solvothermal Synthesis, Acs Energy Lett, 3 (2018) 1698-1707.

[164] Y. Liu, X. Liang, L. Gu, Y. Zhang, G.-D. Li, X. Zou, J.-S. Chen, Corrosion engineering towards efficient oxygen evolution electrodes with stable catalytic activity for over 6000 hours, Nat Commun, 9 (2018) 2609.
[165] X.-X. Jiang, J.-Y. Xue, Z.-Y. Zhao, C. Li, F.-L. Li, C. Cao, Z. Niu, H.-W. Gu, J.-P. Lang, Ultrathin sulfate-intercalated NiFe-layered double hydroxide nanosheets for efficient electrocatalytic oxygen evolution, RSC Advances, 10 (2020) 12145-12150.
[166] L. Yu, J.F. Yang, B.Y. Guan, Y. Lu, X.W. Lou, Hierarchical Hollow Nanoprisms Based on Ultrathin Ni-Fe Layered Double Hydroxide Nanosheets with Enhanced Electrocatalytic Activity towards Oxygen Evolution, Angewandte Chemie International Edition, 57 (2018) 172-176.
[167] X. Lu, C. Zhao, Electrodeposition of hierarchically structured three-dimensional nickel–iron electrodes for efficient oxygen evolution at high current densities, Nat Commun, 6 (2015) 6616.
[168] Q. Zhao, J. Yang, M. Liu, R. Wang, G. Zhang, H. Wang, H. Tang, C. Liu, Z. Mei, H. Chen, F. Pan, Tuning Electronic Push/Pull of Ni-Based Hydroxides To Enhance Hydrogen and Oxygen Evolution Reactions for Water Splitting, Acs Catal, 8 (2018) 5621-5629.
[169] H. Xu, B. Wang, C. Shan, P. Xi, W. Liu, Y. Tang, Ce-Doped NiFe-Layered Double Hydroxide Ultrathin Nanosheets/Nanocarbon Hierarchical Nanocomposite as an Efficient Oxygen Evolution Catalyst, Acs Appl Mater Inter, 10 (2018) 6336-6345.
[170] M.S. Wu, C.H. Yang, Electrochromic properties of intercrossing nickel oxide nanoflakes synthesized by electrochemically anodic deposition, Appl Phys Lett, 91 (2007) 033109.

국문초록

근래 세계는 점점 심각해지는 기후변화, 자원민족주의, 전쟁 등에 대응하기 위해서 화석연료 위주의 과학기술로부터 벗어나 보다 친환경적이고 지속가능한 과학기술 개발에 박차를 가하고 있다. 이를 위해서는 저렴하면서도 매우 효율 높은 전기화학 촉매 개발이 선행되어야 하는데, 이에는 촉매의 근본적인 전기화학적 성질에 대한 올바른 이해가 필요하다. 본 학위논문에서는 전기화학 촉매의 근본적 이해를 돕기 위한 두 가지 주제에 대해 서술하겠다.

첫번째로 나노다공성 전기화학 촉매의 구조에 의한 촉매 효율 변화에 대해 상술하겠다. 먼저 정교하고 정의된 촉매구조를 개발하기 위해 균일한 구조를 갖는 인듐 주석 산화물 나노육면체를 합성하였다. 다음, 나노육면체의 자가조립을 통해 작은 크기의 집합체를 유도하였다. 작은 크기로 뭉친 나노육면체는 자가조립에 의해 크기가 매우 작으면서도 균일한 동공을 갖도록 유도했으며, 이러한 나노육면체 집합체가 얼기설기 뭉치면서 생긴 더 큰 동공을 통해 다중-동공 형태의 나노다공성 전극을 제작할 수 있었다. 이렇게 제작된 나노다공성 전극에서 홀 전자 전달 반응의 대표격인 철 이온의 산화환원을 살펴본 결과, 나노다공성 전극에서의 촉매 활성이 단순 평면 전극에 비해 매우 뛰어남을 관찰했다. 이를 통해 전극의 구조적 특성으로 인해 단순히 전극 면적이 늘어나는 것 이상으로 반응성이 향상됨을 알 수 있었다. 반면, 다중 전자 전달 반응으로 아스코르브산 산화반응과 산소환원반응을 살펴본 결과, ITO의 전기화학적 비활성의 영향으로 인해 이전에 관찰했던 구조적인 효과가 거의 나타나지 않는다는 것을 관찰했다. 이로부터 효율적인 전극 개발에 있어서는 전극의 구조도 중요하지만 특정 반응에 대한 전극 물질의 활성도 또한 중요한 역할을 한다는 것을 유추할 수 있었다.

두번째로 니켈 철 산화물의 산화도금에 있어서 음이온이 끼치는 영향에 대해 상술하겠다. 니켈 철 산화물은 매우 유망한 물 산화 전기화학 촉매임에도 불구하고, 이전까지 개발된 산화도금 방법으로는 최대 촉매 효율을 얻지 못하였다. 전기화학 수정진동자저울을 적용한 실험방법을 이용해 니켈 철 산화물의 산화도금을 자세히 연구한 결과, 금속 전구체의 음이온과 용액 속 음이온 모두 산화도금에 지대한 영향을 끼친다는 것을 알아낼 수 있었다. 음이온은 단순 완충용액의 역할을 해서 pH를 유지시기는 것뿐만 아니라 산화도금 중 생성되는 수소이온을 빠르게 잡아내 반응성을 유지시켜준다는 것을 알 수 있었다. 이를 바탕으로 수정된 새로운 산화도금 방법으로 합성된 니켈 철 산화물 촉매는 이전까지 개발된 다른 니켈 철 산화물 촉매 중에서도 매우 뛰어난 촉매 효율을 보여줬다. 이러한 발견은 산화도금에 있어서 그 동안 외면되어 자세히 관찰되지 않은 근본적인 것들도 매우 큰 영향을 줄 수 있기에 앞으로의 촉매 합성에 있어서는 이런 작은 부분들도 놓치지 않고 살펴보아야 한다는 점을 시사한다.